Lifetime Distributions for Unidirectional Fibrous Composites under Creep-Rupture Loading

S. Mahesh (mahesh@lanl.gov)
Materials Science and Technology Division,
Los Alamos National Laboratory, Los Alamos NM 87545.

S. L. Phoenix (slp6@cornell.edu)
Department of Theoretical and Applied Mechanics,
Cornell University, Ithaca NY 14853.

Abstract. Monte-Carlo simulations and theoretical modeling are used to study the statistical failure modes and associated lifetime distributions of unidirectional 2D and 3D fiber-matrix composites under constant load. Within the composite the fibers weaken over time and break randomly, and the matrix undergoes linear viscoelastic creep in shear. The statistics of fiber failure are governed by the breakdown model of Coleman (1958a), which embodies a Weibull hazard functional of fiber load history imparting power-law sensitivity to fiber load with exponent ρ, and Weibull lifetime characteristics with shape parameter β. The matrix has a power-law creep compliance in shear with exponent α. Fiber load redistribution at breaks is calculated using a shear-lag mechanics model, which is much more realistic than idealized rules based on equal, global or local load-sharing. The present study is concerned only with the "avalanche" failure regime discussed by Curtin and Scher (1997) which occurs for sufficiently large ρ, and whereby the composite lifetime distribution follows weakest-link scaling. The present Monte-Carlo failure simulations reveal two distinct failure modes within the avalanche regime: For larger ρ, where fiber failure is very sensitive to load level, the weakest link volume fails in a "brittle" manner by the gradual growth of a cluster of mostly contiguous fiber breaks, which then abruptly transitions into a catastrophic crack. For smaller ρ, where this load sensitivity is much less, the weakest link volume shows "tough" behavior, i.e., distributed damage in terms of random fiber failures until failure of a critical volume and its catastrophic extension. The transition from brittle to tough failure mode for each ρ within the avalanche regime is gradual and depends on the matrix creep exponent α and Weibull exponent β. Also, as α increases above zero the sensitivity of median composite lifetime to load level increasingly deviates from power-law scaling known to occur for the elastic matrix case, $\alpha = 0$. By probabilistic modeling of the dominant failure modes in each regime we obtain distribution forms and various scalings for damage growth, and for carefully chosen sets of parameter values we analytically extend simulation results on small composites (limited by current computer power) to more realistic sizes. Our analytical strength distributions are applicable for $\rho > 2$ in 2D, and $\rho \gtrapprox 4$ in 3D. The 2D bound coincides with the avalanche-percolation threshold derived by Curtin and Scher (1997) using entirely different arguments.

1. Introduction

The failure of a component after spending considerable time under constant load is called stress-rupture or creep-rupture. In multi-phase materials, time dependence in the failure process may result from locally growing, randomly distributed flaws within the stiff, primary, load-bearing phases leading to microcracks spanning such phase elements, or at phase boundaries leading to slip or cavitation. Both cause local stress loss and redistribution to nearby phase elements, thus accelerating flaw growth and microcracking within them. Eventually, several microcracks may link to from a growing catastrophic crack. One or more of the phases may also be susceptible to more homogeneous creep in tension or shear, also altering this stress redistribution over time. Thus microcracks may become growing voids observed as global material volume increases over time before void linking and collapse. Experimentally observing and modeling the breakdown phenomena and critical event times during creep-rupture is technologically difficult. For instance, a given material system may exhibit ductile-like behavior where distributed void initiation and growth appears globally as primary, secondary and then tertiary creep that with ultimate localization and collapse. Yet relatively small changes in values of constitutive parameters governing individual phase behavior (often connected with temperature, environmental factors, processing history and local geometry effects) can cause abrupt transitions to brittle-like behavior with much less global creep, no tertiary creep, and thus, little warning of impending component failure. Furthermore, whether a ductile or brittle-like failure mode is observed may depend on the applied load level as well as the component geometry and material volume sustaining the load.

At the same time creep-rupture lifetime statistics for replicated tests on laboratory coupons typically exhibit large variability, and the shapes of the lifetime distributions are strongly dependent on load level, material volume and whether ductile or brittle-like behavior has occurred. Engineers typically design components for long life (decades) and extremely low probabilities of failure (e.g., $P_f = 10^{-6}$ to $P_f = 10^{-9}$) depending on life-safety constraints. The issue is one of sizing the component to achieve a suitable load level for the desired reliability goal. For several reasons this is not achievable by physical testing alone: First, components may be much larger than laboratory test coupons for which multiple test fixtures are available to gather creep-rupture data. Second, the number of such fixtures can never be enough to provide sufficient data to access the high reliability regime, especially since several fixed load levels may be necessary to investigate lifetime

sensitivity to load. Third, testing must be done in real time, which cannot be fully completed in advance of putting components into service. Thus to predict reliable component life engineers must resort to accelerated testing methods, critical examination of specimens removed from service, and ultimately, data extrapolation. Thus it is crucial to have available sophisticated, validated models that are based on actual material microstructures and the micromechanics and statistics of failure processes. These may combine analytical and Monte Carlo simulation approaches.

Unidirectional fiber-matrix composites are of great interest, not only because they are high performance materials in their own right, but also because they serve as model materials for study of the creep-rupture processes described above. Examples of such systems are: (i) polymer-matrix composites such as continuous aramid, PBO, carbon (graphite), glass and PIPD (M5) fibers embedded in epoxy, polyester, nylon or polyimide resins (ii) metal-matrix composites such as silicon carbide or alumina fibers in an aluminum or titanium matrix, and (iii) brittle-matrix composites such as silicon carbide or alumina fibers in a silicon carbide or silicon nitride ceramic, or an LAS glass matrix.

The fibers are the stiff, main load-bearing phase with randomly distributed flaws that grow over time and result in sudden fiber breaks where tensile load is unsupported. This strength degradation at flaws is highly stochastic and depends on the local stress history. Breakdown originates at the nanoscale in the form of thermally activated inter-molecular slipping and/or bond breaking eventually culminating in micron scale cracks that grow and sever the fiber. The matrix serves mainly to redistribute the lost load at breaks onto fibers in their vicinity, overloading them above the original far-field applied load. In polymer matrices the thermally activated sliding motion of polymer chains is manifest as viscoelastic creep in shear. In metals, shear creep results from thermally activated dislocation motion and material transport mechanisms along interfaces. Such creep leads to increasing, relative, longitudinal displacements between the fibers that causes changing profiles of stress redistribution. Relative fiber displacement may also result from time-dependent debonding and slip at the fiber-matrix interface. Though occurring with all matrices, this is the primary mechanism of time-dependence of load transfer in glass and ceramic matrices. Although nominally brittle and stiff, such matrices are much weaker than the fibers in tension and undergo quasi-periodic cracking transverse to the fibers, greatly reducing the tensile matrix stress. This converts them mainly to a medium of load transfer from fiber to fiber through shear, though the load transfer tends to be more dispersed than for polymer and metal matrices.

As we will see, depending on the stochastic parameters of fiber break generation, the matrix creep exponent, and the fiber array geometry, the failure process may appear as one of two basic statistical modes: The first is brittle-like and involves very little distributed damage (in terms of fiber breaks) before a few small growing cracks of contiguous fiber breaks appear, one of which becomes dominant and catastrophic; The second is more ductile-like wherein composite failure results from the accumulation of distributed damage before local instability that spreads to cause collapse. Predicting the tendency toward a particular mode and associated lifetime distribution is a difficult task and certainly should not be forced 'a priori' or inadvertently result from simplifying assumptions. On the other hand, comprehensive inclusion of all the above failure mechanism details, is not yet possible either from a mechanics or a stochastic process standpoint.

In our analytical modeling, we will therefore idealize the composite structure and failure processes in terms of progressive fiber failures and load redistribution in shear, though still preserving key physical aspects and statistical. These simplifications will render the problem analytically tractable. At the same time we will develop Monte Carlo simulation models that make far fewer idealizations, but can only be implemented on composites of small size, or large composites with small periodic cells. The key goal will be to integrate the analytical and simulation models to make predictions about much larger composites. These will include the statistical mode of composite failure in creep-rupture, the mathematical character of the associated lifetime distributions, and the scaling laws relating load level to lifetime as well as to certain intermediate events. These quantities will be functions of composite volume and various model parameters.

Specifically we focus on the lifetime statistics for a unidirectional fiber-matrix composite consisting of aligned elastic fibers embedded in a linearly viscoelastic matrix and subjected to a constant load in tension. The stochasticity of fiber failure will be governed by the breakdown model of Coleman (1958a), and in shear the matrix will have a power-law creep compliance with exponent α. When breaks occur, fiber load redistribution will be calculated using a shear-lag mechanics model, which is much more realistic than idealized rules based on equal, global or local load-sharing.

We will calculate the composite lifetime distribution in two steps: Through Monte-Carlo simulations on small specimens, we first map the parametric regions governing fiber breakdown statistics and matrix creep rates to the dominant observed composite failure modes. Then we construct probabilistic failure models of these dominant modes to analytically deduce composite lifetime distributions for realistically

sized composites. This procedure is necessarily somewhat speculative since the Monte-Carlo simulation cell sizes are limited by computational constraints, and therefore may suffer from finite size effects. However, given present computational power, and the infeasibility of large scale numerical replications ($\sim 10^7$ tests) needed to assure deep tail levels of reliability ($\sim 10^{-6}$), the present approach is the best available in our judgment. In the remainder of the introduction we describe the geometry of the model and anticipated failure evolution features in more detail. With this perspective we review pertinent literature and how it bears on the modeling and analysis approaches we take.

1.1. The Idealized Unidirectional Composite

Our idealized composite consists of a parallel array of n stiff, brittle, elastic fibers of cross sectional area $A_{\rm f}$ and length L, embedded in a flexible, perfectly bonded, elastic or viscoelastic matrix. Two fiber arrays are considered: a linear array forming a 2D planar composite ("2D array") and a hexagonal array forming a 3D composite ("3D array"), as shown in Figure 1. Fibers in the 2D array are indexed from left to right by a single integer coordinate ℓ whereas in the 3D array, each fiber is identified by its ℓ and m integer coordinates. We assume periodic boundary conditions both longitudinally and transversely, or equivalently, the composite has periodic cell structure. We assume that the fibers carry virtually all the load and the composite is loaded by applying a far-field, tensile load p_∞ to each fiber.

The matrix locally transfers load from broken to intact fibers through shear. In Section 2 this is idealized in terms of a classic shear-lag model where the matrix has a linear, power-law creep compliance with exponent α. The model will begin with general geometric features but ultimately the fibers will be in the 2D and 3D arrays above.

In Section 3 we describe the stochastic fiber breakdown model of B. D. Coleman (1958a), which embodies a Weibull hazard functional of fiber load history imparting power-law sensitivity to fiber load with exponent ρ and Weibull lifetime under constant fiber load with shape parameter β. The lifetime of a fiber element is thus determined by the stochastic breakdown of its weakest flaw, which depends on its load history.

When a constant tensile load of p_∞ per fiber is applied to a specimen, fibers fail randomly in succession at the first few weakest flaws, and the matrix surrounding each break transfers the lost fiber load to neighboring fibers through shear deformation. This stress transfer occurs over a length scale of a few fiber diameters, which in general grows in time. In the simulations, which involve periodic cells, it is important to

chose the cell length to greatly exceed the length scale of load transfer by the time of composite collapse. By the same token the transverse cell size must greatly exceed the size scale of break interaction and localized damage development that ultimately results in the collapse of some characteristic volume that becomes a catastrophic crack. How to scale the results of small periodic cells to composites of large volume becomes the task of the analytical models developed in later sections.

Many of the steps required in fully developing the model are technically complex and difficult to condense while keeping the line of derivation comprehensible to readers interested in all the details. Thus we place many of the technical discussions in Appendices and concentrate on the key themes and results that are ultimately most important.

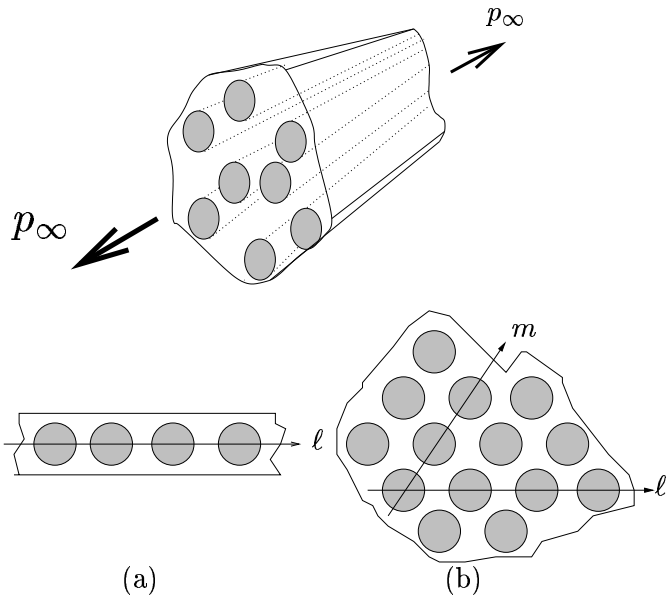

Figure 1. Two fiber arrays modeled: (a) planar array and (b) hexagonal array. The far-field stress applied to the fibers is p_∞. Fibers in the 2D array are indexed by a single integer ℓ whereas in the 3D array, they are indexed by the ordered pair (ℓ, m).

1.2. Results from Previous Literature

Previous literature may be classified into two categories. The first consists of work on fiber lifetime models and determining asymptotic lifetime distributions for equal load-sharing bundles by Coleman (1956, 1957a, 1957b, 1958b, 1958a), and Phoenix (1978). Equal load sharing assumes that the load dropped by broken fiber all along its length is equally divided among all the surviving fibers. We detail Coleman's

fiber lifetime formulation in Section 3 and Phoenix's conclusion that the lifetime of a bundle of Coleman fibers is asymptotically (as bundle size grows to infinity) normally distributed in Section 4.1. Ibnabdeljalil and Phoenix (1995) study the lifetime distribution of composites by means of Monte Carlo simulations where global fiber load sharing is assumed. This is a more continuous version of equal load sharing in which the fiber stress lost at a break is gradually regained over a certain characteristic distance along the fiber on each side. Composites much longer than this characteristic distance typically have lifetime distributions that have a weakest link structure in terms of links with log-normal lifetime (which is also normal in the limit of extremely large bundles).

The second category of work relates to local load-sharing composites. Here, fiber stress concentrations next to a transverse array of fiber breaks (a discrete crack) are largest at the crack tip and fibers further away feel little overload. The asymptotic lifetime in such a case is not normal or log-normal. Instead it has a weakest link basis in terms of a certain characteristic lifetime distribution as Tierney (1980, 1982) and Phoenix and Tierney (1983) have shown. These authors consider idealized load sharing rules, which in the case of a planar fiber array translates to the stress concentration on the two fibers adjacent to an r-cluster of breaks being equal to $1+r/2$. Newman and Phoenix (2001) have studied the statistical lifetime problem under this assumption, for the entire range of fiber lifetime sensitivity to load history (parameterized by ρ, and described in Section 3), and found a sharp transition in failure mode at $\rho = 1$. While this idealization captures the important characteristic of crack formation and propagation, it is far too severe. Hedgepeth (1961) and Hedgepeth and Van Dyke (1967) give a mechanically consistent method of calculating the fiber stress state in a composite with breaks. Their shear-lag based analysis results in more realistic stresses but was restricted to the case where both the fiber and matrix are elastic. It was extended by Lagoudas et al (1989) to the case where the matrix is viscoelastic and all the fiber breaks lie in a single plane perpendicular to the fiber direction. Beyerlein and Phoenix (1998), however, give a shear-lag methodology to compute the stress state in the composite under arbitrary arrangements of breaks. To our knowledge, lifetime studies of Hedgepeth composites with fibers undergoing time-dependent breakdown and an elastic or viscoelastic matrix have not been done and we address that question here.

Curtin and Scher (1991, 1997), and Curtin et al (1997) have extensively studied the time-dependent failure of spring networks wherein damage resembles cracks in Hedgepeth composites in the scaling of stress concentration ahead of a cluster of fiber breaks. They find two

regimes of composite failure: an avalanche regime for $\rho > 2$, wherein composite failure occurs by a catastrophically growing volume of local damage, and a percolation regime for $\rho \leq 2$, wherein composite failure is essentially global, and occurs through the formation of a percolating cluster of fiber breaks. Recently Goda (2001) has considered this problem directly in the framework of Hedgepeth with similar results.

A class of problems closely related to the lifetime problem is the strength problem where fibers have random strengths according to some prescribed distribution function and the composite is loaded quasi-statically under increasing tension. The strength distribution of the composite is usually sought and this can be viewed as a limiting case of the lifetime version and affords insights into the dominant composite failure modes near the limit. In this connection we note the works of Beyerlein and Phoenix (1997a, 1997b), Landis et al. (2000), Wu and Leath (2000), and Mahesh et al. (1999) and Goda (2003).

2. Shear-Lag Based Load Sharing in Unidirectional Arrays

We now extend the method of Beyerlein et al. (1998) and Landis et al. (2000) to calculate the stress state around finite patterns of breaks in a parallel fiber array within a viscoelastic matrix. We use periodic boundary conditions, both transversely and longitudinally, which enables us to consider a periodically repeating *unit cell* and the fiber and matrix stresses therein. A key issue will be determining a cell size sufficiently large for accurate failure probability calculations for much larger composites, especially under high reliability requirements.

2.1. Governing Equations and Boundary Conditions

We consider a collection of $n < \infty$ parallel fibers in an arbitrary array within the matrix, where x is the coordinate along the fiber direction. According to Hedgepeth's shear-lag assumptions, fibers deform in pure tension and the matrix deforms in pure shear. The fibers are loaded uniformly in simple tension in the far field under p_∞ per fiber for $t \geq 0$, and the load is zero for $t < 0$. We refer to the fiber direction as longitudinal and to planes perpendicular to it as transverse. We assume the fibers are linearly elastic with tensile modulus E_f cross-sectional area A_f. We let $p_i(x,t)$ and $u_i(x,t)$ be the tensile load and displacement, respectively, in fiber i at position x and time t, where $1 \leq i \leq n$. Note that $p_i(x,t) = u_i(x,t) = 0$ for $t < 0$ and $p_i(x,t) = p_\infty$ when all fibers are intact and $t \geq 0$. If some fibers have breaks, however, the lost loads around them must be redistributed to intact fibers through

matrix shear stresses. We let the shear force per unit length transmitted from fiber j to fiber i at (x,t) be $q_{ij}(x,t)$. Force equilibrium on a fiber element of length dx requires

$$A_{\rm f}\frac{\partial p_i}{\partial x}dx + \left(\sum_{j=1}^{n} q_{ij}\right)dx = 0, \qquad i = 1,2,\ldots,n, \tag{1}$$

and Hooke's law for the fiber gives

$$p_i(x,t) = E_{\rm f}A_{\rm f}\frac{\partial u_i}{\partial x}(x,t). \tag{2}$$

To relate q_{ij} to the relative displacement of the fibers we assume the matrix is viscoelastic with a power-law creep compliance in shear,

$$J_{\rm m} = J_{\rm e}\left(\frac{t}{t_{\rm cm}}\right)^{\alpha}, \quad t \geq 0, \tag{3}$$

where α is the creep exponent limited to $0 \leq \alpha \leq 1$, $t_{\rm cm}$ is a time constant and $J_{\rm e}$ is a compliance constant with an interpretation given shortly. If $G_m(t)$ is the corresponding relaxation modulus, it can be shown using Laplace transforms and the fact $s^2\bar{J}_{\rm m}(s)\bar{G}_{\rm m}(s) = 1$ that

$$G_{\rm m}(t) = G_{\rm e}\left(\frac{t_{\rm cm}}{t}\right)^{\alpha}, \quad t \geq 0 \tag{4}$$

where $G_{\rm e}$ and $J_{\rm e}$ are related according to

$$G_{\rm e} = 1/(J_{\rm e}\Gamma(1+\alpha)\Gamma(1-\alpha)). \tag{5}$$

By linear viscoelasticity

$$q_{ij}(x,t) = \int_0^t G_{\rm m}(t-v)\varphi_{ij}\frac{\partial}{\partial v}(u_j(x,v) - u_i(x,v))dv. \tag{6}$$

In Eq. (6), $\varphi_{ij}(u_j(x,v) - u_i(x,v))$ is the matrix displacement in shear and q_{ij} represents the shear force on fiber i due to fiber j as a hereditary integral. φ_{ij}, $i \neq j$ is a non-negative non-dimensional geometric parameter that quantifies the proximity of fibers i and j.

Eq. (3) assumes the creep compliance is a simplification of

$$J'_{\rm m}(t) = J_{\rm e}(1 + t/t_{\rm cm})^{\alpha}, \tag{7}$$

which also accounts for instantaneous elastic shear response of the matrix, with compliance $J_{\rm e}$. We use Eq. (3) because it is more amenable to algebraic manipulations than Eq. (7). As $t/t_{\rm cm} \to \infty$, the two forms converge, but they especially differ for times $0 < t < t_{\rm cm}$. However,

the instantaneous stress and displacement response of Eq. (7) is well approximated by Eq. (3) upon setting $t = t_{\rm cm}$.

In simulating failure in 2D planar arrays, we impose both lateral and longitudinal periodic boundary conditions on the n fibers. For the former, fibers $\ell = 1$ and $\ell = n$ are adjacent. Also φ_{ij} can be expressed in terms of composite geometric parameters. Let the effective matrix width between fibers be w, and the matrix thickness (perpendicular to the plane of the fibers) be h. We assume h is also the main fiber cross-sectional dimension. A matrix bay exists only between adjacent fibers $\ell = i$ and $\ell = i + 1$, so the effective shear force per unit length $q_{i,j}$ is

$$q_{ij}(x,t) = \int_{-\infty}^{t} G_{\rm m}(t-v)\frac{h}{w}\frac{\partial}{\partial v}(u_j(x,v) - u_i(x,v))dv, \quad \text{if } |i-j| = 1 \tag{8}$$

and $q_{ij}(x,t) = 0$ otherwise. Thus for the 2D array, we take

$$\varphi_{ij} = \begin{cases} h/w & \text{if } |i-j| \mod n = 1, \\ 0 & \text{otherwise} \end{cases} \tag{9}$$

when $i \neq j$, and so the fiber indexing may be extended to an infinite 2D array with periodic cells. We specify φ_{ii} later.

In simulating failure in 3D hexagonal arrays, the transverse periodic boundary conditions result in unit cells each with n fibers and a rhombus shaped transverse cross-section of side length $\sqrt{n}$ (so n must take certain values). Each edge of the rhombus is effectively contiguous with the edge opposite to it. We label the fiber at $(\ell, m) = (0,0)$ as 1, then we label the remaining fibers in the rhombus cell with integers in sequence, first proceeding along the $m = 0$ row, then the $m = 1$ row and so on until the $m = \sqrt{n} - 1$-th row. Thus, the fiber with label i is located at $\ell = i \mod \sqrt{n}$ and $m = \lfloor i/\sqrt{n} \rfloor$. Conversely, the fiber at (ℓ, m) is indexed by $\ell\sqrt{n} + m + 1$.

A similar argument to that in 2D is carried out for φ_{ij}, with w representing an effective matrix thickness. Thus

$$\varphi_{(\ell_1,m_1),(\ell_2,m_2)} = \begin{cases} h/w & \text{if } \max((\ell_1 - \ell_2) \mod \sqrt{n}, (m_1 - m_2) \mod \sqrt{n}) = 1, \\ 0 & \text{otherwise} \end{cases} \tag{10}$$

where (ℓ_1, m_1) are the coordinates of fiber i and (ℓ_2, m_2) are the coordinates of fiber j and $i \neq j$. Again we specify φ_{ii} later.

These two arrays are used in the following sections. However, the shear-lag methodology in the remainder of this section applies to arbitrary fiber arrays provided φ_{ij} is chosen appropriately.

Combining Eqs. (1), (2), and (6) yields the governing equation

$$E_{\rm f}A_{\rm f}\frac{\partial^2 u_i(x,t)}{\partial x^2}+\int_0^t G_{\rm m}(t-v)\frac{\partial}{\partial v}\left(\sum_{\substack{j=1\\ j\neq i}}^{n}\varphi_{ij}u_j(x,v)-\left(\sum_{j=1}^{n}\varphi_{ij}\right)u_i(x,v)\right)dv = 0, \quad i=1,2,\ldots,n. \tag{11}$$

Defining

$$\varphi_{ii}=-\sum_{j=1,i\neq j}^{n}\varphi_{ij}, \tag{12}$$

Eq. (11) can be shortened to

$$E_{\rm f}A_{\rm f}\frac{\partial^2 u_i(x,t)}{\partial x^2}+\int_0^t G_{\rm m}(t-v)\left(\sum_{j=1}^{n}\varphi_{ij}\frac{\partial u_j(x,v)}{\partial v}\right)dv=0. \tag{13}$$

For the transverse boundary conditions to Eq. (13), let B be the set of r breaks in the periodic patch at time t. We locate each break by its fiber number, i and its x coordinate. Thus, we let

$$B=\{(i_1,x_1),(i_2,x_2),\ldots,(i_r,x_r)\}. \tag{14}$$

For the longitudinal periodicity, the fiber breaks occur along the fiber direction with periodicity L. That is, if $0\le x_k<L$, $k=1,\ldots,r$, breaks repeat at $x_k\pm jL$, $j=1,2,\ldots$. The case of infinite boundary conditions is retrieved by letting $L\to\infty$. If L is finite, periodicity demands that for $i=1,2,\ldots,n$

$$p_i(x=0,t)=p_i(x=L,t), \qquad t\ge 0, \tag{15}$$

for traction continuity in the fiber direction across unit cells. Also, letting $c(t)$ be a function continuous in t, then for some $c(t)$,

$$u_i(0,t)=u_i(L,t)+c(t), \quad t\ge 0, \quad (i,0)\notin B \tag{16}$$

for displacement continuity in the absence of boundary cracks. Thus $c(t)$ is independent of i but in general must depend on the position and number of fibers. By way of the traction free boundary condition at fiber breaks, we have

$$p_{i_k}(x_k,t)=E_{\rm f}A_{\rm f}\frac{\partial u_{i_k}(x_k,t)}{dx}=0, \qquad (i_k,x_k)\in B, \quad k=1,\ldots,r. \tag{17}$$

Finally, in order that the applied load be carried by all fibers we need

$$\sum_{i=1}^{n} p_i(x,t) = np_\infty, \quad t \geq 0, \quad 0 \leq x \leq L. \tag{18}$$

2.2. Results and Approximations from Shear-Lag Analysis

The solution methodology of the governing equations in the preceding section is described in Appendix A. The explicit solution for the time evolution of stresses in a composite with a single break can be found in Eq. (136), and is given in terms of the normalized time $\tau = t/t_{\rm cm}$ (see Eq. (103)), and normalized axial coordinate $\xi = x/\delta_{\rm v}$ (see Eq. (102)). $\delta_{\rm v}$ is a viscoelastic characteristic length scale and is approximately the length of the unloading zone around a fiber break at time $t_{\rm cm}$ after its formation.

It is clear by examining Eq. (136) that the similarity variables

$$z = \frac{\xi}{\tau^{\alpha/2}} \qquad \text{and} \qquad z' = \frac{\mathfrak{L} - \xi}{\tau^{\alpha/2}} \tag{19}$$

are key. In terms of these variables, if $\mathbf{V}'$ denotes the normalized displacement field over and above uniform stretch, the normalized *overstress* field due a single break (see Eq. (137)) is

$$\begin{aligned} \frac{\partial \mathbf{V}'}{\partial \xi} = \Bigg\{ & \sum_{i=2}^{n} \mathbf{C}_i \frac{\lambda_i}{\sqrt{\Gamma(1+\alpha)}} \\ & \times \left[-\exp\left(-\frac{\lambda_i \mu z}{\sqrt{\Gamma(1+\alpha)}} \right) - \exp\left(\frac{\lambda_i \mu z'}{\sqrt{\Gamma(1+\alpha)}} \right) \right] \Bigg\}, \end{aligned} \tag{20}$$

where $\mathbf{C}_i \lambda_i / \Gamma(1+\alpha)$ are scaling vectors (see Appendix A.2). Adding a uniform normalized stretch of ξ, the actual displacement field is given by $\xi + \mathbf{V}'$, and adding normalized applied stress of 1, the stress field is $1 + \partial \mathbf{V}'/\partial \xi$. Taking $\mathfrak{L} \to \infty$, the dependence of the stress state on ξ and τ now enters exclusively through the similarity variable z. Also as n is increased, this normalized stress solution quickly approaches that of Beyerlein et al. (1998) for $n = \infty$ obtained by an influence function approach. In the rest of this section, this condition is met. In fact, convergence to the $n = \infty$ solution is numerically complete if we take $n = 400$ in the presence of fewer than 20 fiber breaks even when contiguous. Hence, the transverse interaction of breaks across unit cells can be neglected.

Henceforth, we will focus solely on the 2D and 3D arrays of Section 1.1 subject to periodic boundary conditions both in the fiber direction and in the transverse plane. We will examine composite stresses

in the presence of certain special break configurations that are useful in the probabilistic modeling in Section 4. The methodology for deducing the stress field in a composite with multiple interacting breaks from the single break influence functions Eq. (20) is given in Appendix A.3.

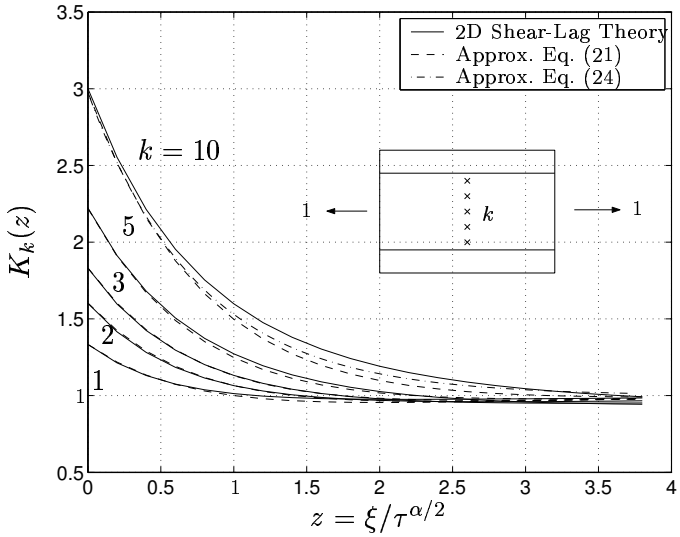

Figure 2. Stress decay in 2D on the fiber adjacent to a cluster of k breaks in the $\xi = 0$ plane. $\mathfrak{L}$ is set to ∞ so there are no longitudinal cluster images. The number of fibers is sufficiently large that the transverse interaction of clusters is negligible.

Figure 2 shows the stress profile so deduced in the fiber adjacent to a transverse cluster of contiguous breaks in a 2D array with $\mathfrak{L} = \infty$. $K_k(z)$ is the stress concentration in the fiber adjacent to the k-cluster located at $\xi = 0$ formed at $\tau = 0$. The approximation

$$K_k(z) \approx \check{K}_k(z) = 1 + (\check{K}_k(0) - 1)(1 - z/\sqrt{k}) \exp(-z) \qquad (21)$$

accurate for small k where

$$K_k(0) \approx \check{K}_k(0) = \sqrt{\frac{\pi k}{4} + 1} \qquad (22)$$

is also shown. (We use ' $\check{}$ ' to denote approximations.) We let ω_k be the "overload length" on the fiber adjacent to a cluster of k breaks, which is the length over which its stress concentration exceeds 1. In 2D, with $\mathfrak{L} = \infty$, we approximately have

$$\omega_k \approx \check{\omega}_k = \sqrt{k}\tau^{\alpha/2}. \qquad (23)$$

A more convenient approximation, superior to Eq. (21) for larger k, is

$$K_k(z) \approx \check{K}_k(z) = 1 + (\check{K}_k(0) - 1) \exp(-z(1 + 1/\sqrt{k})). \qquad (24)$$

Unlike Eq. (21), Eq. (24) however results in $K_k(z) > 1$, for all z.

A similar observation holds for the 3D array if we identify a *tight cluster* as the 3D counterpart of the cluster of k contiguous breaks in 2D. A tight cluster is an ordered collection of fiber breaks in a transverse plane wherein each successive break occurs on an intact fiber subject to the largest overload due to the previous, smaller cluster. Figure 3 depicts an ordered 10-break, tight cluster together with the peak stress concentrations on the most heavily loaded peripheral intact fibers next to previous smaller clusters. This sequence is not monotonic. For instance, $k = 6$ fails at a higher stress concentration than $k = 7$. This is due to the jaggedness of the tight cluster as it grows; the $k = 7$ fiber is surrounded by three broken fibers as opposed to the $k = 8$ fiber, which has two broken neighbors. Aspects of these irregularities are discussed in detail in Mahesh et al (1999) and accounting for them will be key to probabilistic modeling of the lifetime distribution.

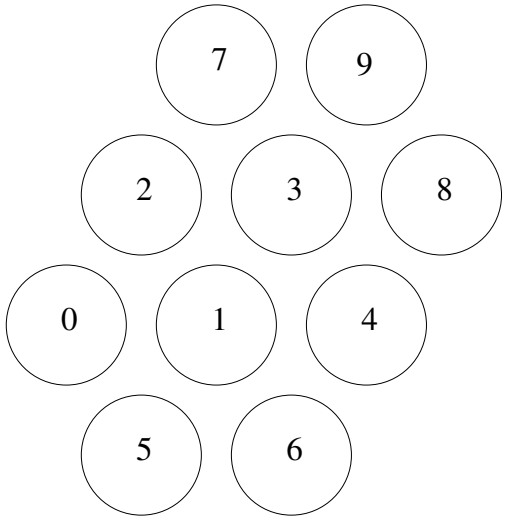

k	$K_k(0)$	$\check{K}_k(0)$
0	1.0000	1.0000
1	1.1046	1.1658
2	1.2337	1.2280
3	1.2828	1.2736
4	1.3205	1.3109
5	1.3644	1.3428
6	1.5889	1.3711
7	1.4107	1.3965
8	1.4596	1.4198
9	1.6163	1.4414

Figure 3. One possible sequence for tight cluster growth to 10 fiber breaks in a hexagonal fiber array. The numbers $(0, 1, 2, \ldots, 9)$ denote the order of fiber breaking. Also included are the associated stress concentrations in the $\xi = 0$ plane if $\mathfrak{L} = \infty$ and their estimates according to Eq. (27).

For the fiber subject to the largest overload from the critical cluster (which may break and extend the cluster), we see in Figure 4 that

$$K_k(z) \approx \check{K}_k(z) = 1 + (\check{K}_k(0) - 1)(1 - 2z/\sqrt[4]{k}) \exp(-2z) \qquad (25)$$

approximates the stress decay on the adjacent fiber away from the cluster plane. The overload length in 3D with $\mathfrak{L} = \infty$ approximately is

$$\omega_k \approx \check{\omega}_k = \tau^{\alpha/2}\sqrt[4]{k}/2. \tag{26}$$

Edge jaggedness of a tight cluster is reflected in the fluctuations of the stress concentrations on its neighbors and hence in the peak value, $K_k(0)$. An accurate approximation for this peak around a *smooth* k-cluster, none of whose neighbors is adjacent to more than two fiber breaks, is given by

$$K_k(0) \approx \check{K}_k(0) = \sqrt{\frac{2\sqrt{k}}{\pi^{3/2}} + 1}. \tag{27}$$

Among clusters of fewer than 20 breaks, $k = 6$, 9, 11, 13, 15, 17 and 18 are not smooth; all the others are. The actual $K_k(0)$ for non-smooth clusters is always somewhat greater than given by Eq. (27). As in the 2D case, for larger k, $K_k(z)$ is better approximated by

$$K_k(z) \approx \check{K}_k(z) = 1 + (\check{K}_k(0) - 1)\exp(-2z(1 + 1/\sqrt[4]{k})). \tag{28}$$

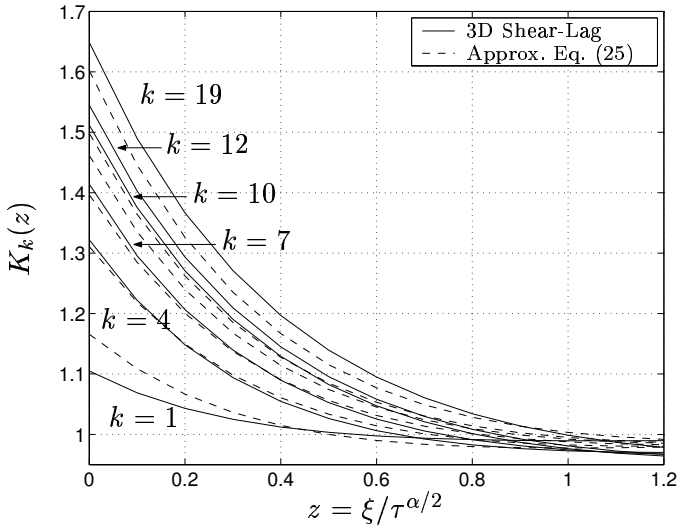

Figure 4. Stress decay in 3D on the fiber adjacent to a cluster of k breaks in the $\xi = 0$ plane. $\mathfrak{L}$ is set to ∞ so there are no longitudinal images of the cluster. The number of fibers in the unit cell is taken large enough that the transverse interaction of clusters is negligible.

The above approximations were derived for $z' = \infty$. However, they are also accurate when $z \ll z'$, especially for small α since $\mu/\sqrt{\Gamma(1+\alpha)}$

in Eq. (20) decreases slowly with increasing α from its peak value of 1 at $\alpha = 0$. Even for $\alpha = 0.5$, $\mu/\sqrt{\Gamma(1+\alpha)} \approx 0.92$. While the stress still decays away from a break according to Eq. (24) in 2D and Eq. (28) in 3D, the approximations can be improved by modifying the expression for $\check{K}_k(0)$ to account for longitudinal interaction between breaks and their periodic images, which finite z' entails. The following modified forms of Eq. (24) and Eq. (28) are good approximations when $\mathfrak{L} < \infty$ but $z \ll z'$; in 2D, in terms of

$$z_L = \frac{\mathfrak{L}}{\tau^{\alpha/2}},$$

we have approximately

$$K_{k,L} \approx \check{K}_{k,L}(0) = \sqrt{\frac{\pi k}{4}\left(1 - \exp(-z_L \psi_1 / k)\right) + 1} \tag{29}$$

and in 3D,

$$K_{k,L}(0) \approx \check{K}_{k,L}(0) = \sqrt{\frac{2\sqrt{k}}{\pi^{3/2}}\left(1 - \exp(-z_L \pi \psi_1 / \sqrt{k})\right) + 1}. \tag{30}$$

When α is small, then these approximations hold with reasonable accuracy if $\mathfrak{L}$ is replaced by $\mathfrak{L}' = e^{-\gamma\alpha/2}\mathfrak{L}/(\tau^{\alpha/2}\Gamma(1+\alpha))$ so long as $\mathfrak{L}' \gg 1$. Figures 5 and 6 compare these approximations against stress concentrations obtained by the shear-lag procedure. Here $\psi_1(\mathfrak{L})$ is a convenient fitting parameter such that as $k \to \infty$, $\check{K}_{k,L}(0) \to \sqrt{\pi\mathfrak{L}\psi_1/4 + 1}$.

When z and z' become comparable in magnitude the simple approximations for $K_k(0)$ in 2D and 3D break down. Figure 7 shows the stress concentration on the fiber next to a single break when $\alpha = 0.5$. For comparison, the time invariant stress concentration for an elastic matrix is also shown. At small times, when $\mathfrak{L}/\tau^{\alpha/2}$ is large, the influence between a break and its longitudinal images is negligible and stresses in the break vicinity are entirely driven by the break. At larger $\tau^{\alpha/2}$, interactions between breaks increase causing the weights (also the break opening displacements) to decrease from their early values. This decreases the fiber overloads adjacent to the break as seen in Figure 7. However, since the stress dropped by the broken fiber must be shifted to survivors in its transverse plane, the overload on more distant fibers will increase. Thus, when $\alpha > 0$, stresses tend to equalize throughout the unit cell as time increases, the speed increasing with α. The influence of periodic boundaries is further enhanced by the presence of large numbers of breaks in each cell since breaks interact with their periodic images besides images of others. This further decreases break opening displacements and the process of stress equalization quickens.

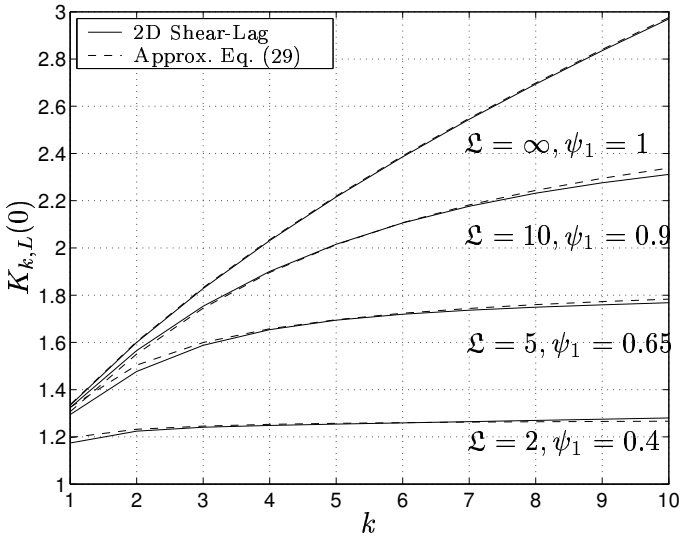

Figure 5. Stress concentration ahead of a k-crack in a periodic 2D bundle of $n = 100$ fibers of length $\mathfrak{L}$. ψ_1 is a convenient fitting parameter in Eq. (29).

Finally we consider the stress enhancements in fibers next to a cluster of k breaks, with two limbs of equal length $k/2$ that are are staggered longitudinally through ξ_s. That is, the cluster consists of breaks on adjacent fibers $1, 2, \ldots, k/2$ at $\xi = 0$ and $k/2+1, k/2+2, \ldots, k$ at $\xi = \xi_s$. In 2D, letting $z_s = \xi_s/\tau^{\alpha/2}$ and $\mathfrak{L} = \infty$, we obtain

$$\check{K}_{k,z_s} \approx \sqrt{\frac{\pi k}{8}\left(1 + \exp(-\psi_2 z_s/\sqrt{k})\right) + 1}, \tag{31}$$

an accurate approximation as Figure 8 shows. In 3D we obtain

$$\check{K}_{k,z_s} \approx \sqrt{\frac{\sqrt{k}}{\pi^{3/2}}\left(1 + \exp(-\psi_2 z_s/\sqrt[4]{k})\right) + 1}. \tag{32}$$

As z_s becomes small, the staggered cluster acts as one aligned cluster.

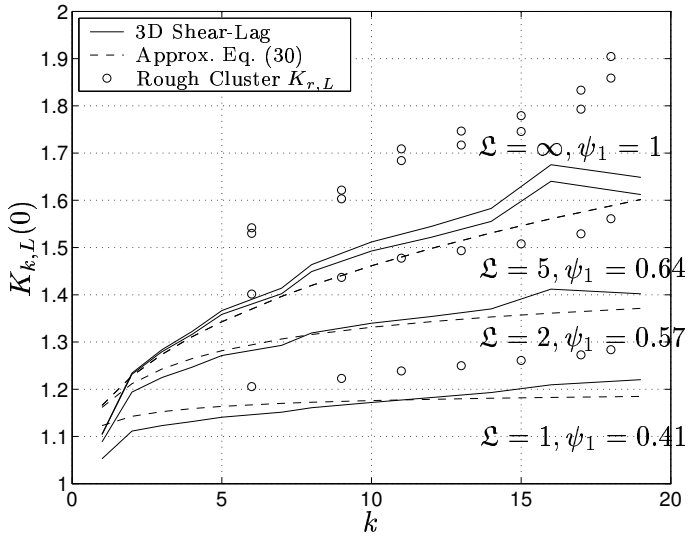

Figure 6. Stress concentration ahead of a k-crack in a periodic 3D bundle of $n = 100$ fibers of length $\mathfrak{L}$. $\psi_1 = \psi_1(\mathfrak{L})$ is the fitting parameter in Eq. (30). Peak stress concentration ahead of rough clusters are shown separately and labeled with $\circ$.

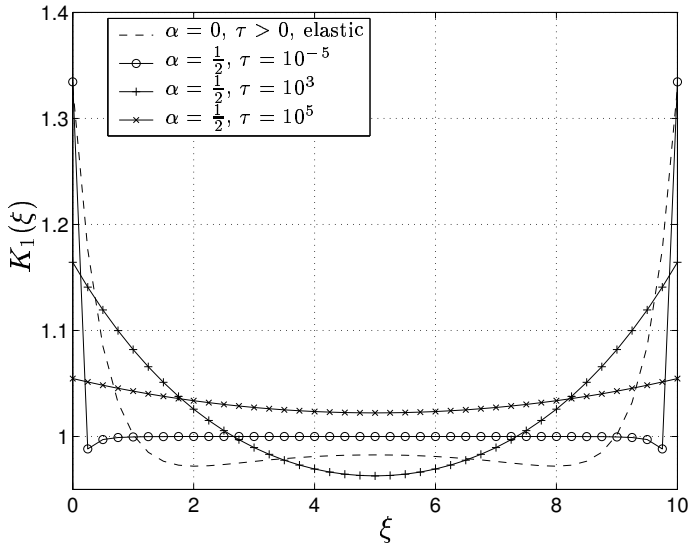

Figure 7. Time variation of the stress profile in the fiber adjacent to a single break in a 2D array of length $\mathfrak{L} = 10$ when $\alpha = 0.5$. For comparison the time-invariant stress profile corresponding to an elastic matrix ($\alpha = 0$) is also shown.

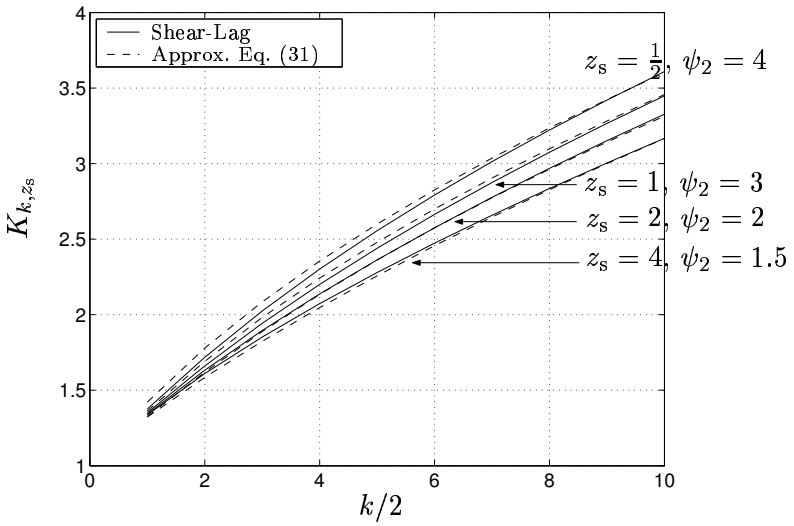

Figure 8. Stress concentration ahead of two adjacent $k/2$-long clusters staggered by $z = \xi_0/\tau^{\alpha/2}$ when $\mathfrak{L} = \infty$. ψ_2 is a fitting parameter used in Eq. (31). Eventually the cluster acts as one aligned cluster

3. Fiber Strength Distribution

Coleman (1958b) introduced a fiber lifetime model whereby the probability that a fiber of length l fails before time t when subjected to the load history $p_u(s)$, $0 \le s \le t$, applied uniformly along its length is

$$F_u(t; p_u(\cdot)) = 1 - \exp\left\{-\Psi\left(l; \int_0^t \kappa(p_u(s))ds\right)\right\}, \tag{33}$$

with the functional forms

$$\Psi(l; y) = \frac{l}{l_0} y^\beta \tag{34}$$

and

$$\kappa(p_u(s)) = \frac{(p_u(s)/p_0)^\rho}{t_{\rm cf}} \tag{35}$$

for Ψ and κ. Here l_0 is the reference gage length and $t_{\rm cf}$ is a characteristic fiber time scale. Incorporating Eq. (34) and in Eq. (33) gives

$$F_u(t; p_u(\cdot)) = 1 - \exp\left\{-\frac{l}{l_0}\left(\frac{1}{t_{\rm cf}}\int_0^t \left(\frac{p_u(s)}{p_0}\right)^\rho ds\right)^\beta\right\}. \tag{36}$$

If the load $p(x,t)$ in a fiber is both position and time dependent, as occurs near a fiber break, a natural generalization of Eq. (36) is

$$F(t, p(\cdot)) = 1 - \exp\left\{-\frac{1}{l_0}\int_0^l dy\left[\frac{1}{t_{\rm cf}}\int_0^t \left(\frac{p(y,s)}{p_0}\right)^\rho ds\right]^\beta\right\}. \tag{37}$$

Normalizing the fiber load at x and t according to

$$\pi(\xi, \tau) = \frac{p(\xi\delta_{\rm v}, \tau t_{\rm cm})}{p_{\rm cf}} = \frac{p(x,t)}{p_{\rm cf}} \tag{38}$$

where

$$p_{\rm cf} = p_0\left(\frac{l_0}{\delta_{\rm v}}\right)^{\frac{1}{\rho\beta}}\left(\frac{t_{\rm cf}}{t_{\rm cm}}\right)^{\frac{1}{\rho}}, \tag{39}$$

Eq. (37) can be rewritten as

$$\mathscr{F}(\tau, \pi(\cdot)) = 1 - \exp\left(-\int_0^\lambda d\xi\left[\int_0^\tau (\pi(\zeta))^\rho d\zeta\right]^\beta\right), \tag{40}$$

where $\lambda = l/\delta_{\rm v}$ is normalized length. Restricting Eq. (40) to the case where the fiber load is uniform, we get the normalized form of Eq. (36)

$$\mathscr{F}_u(\tau, \pi(\cdot)) = 1 - \exp\left(-\lambda\left[\int_0^\tau (\pi_u(\zeta))^\rho d\zeta\right]^\beta\right) \tag{41}$$

where $\pi_u(\tau) = p_u(t)/p_{\rm cf}$. According to Eq. (41) a fiber element of unit normalized length ($\lambda = 1$) loaded uniformly for unit normalized time ($\tau = 1$) under unit normalized load ($\pi_u = 1$) has probability $1 - 1/e$ of failure. Denoting the normalized far field load by $\pi_\infty = p_\infty/p_{\rm cf}$, then

$$\pi_i(\xi, \tau) = \sigma_i(\xi, \tau)\pi_\infty \tag{42}$$

relates the normalized fiber load $\pi(\xi, \tau)$ to the fiber stress concentration $\sigma_i(\xi, \tau)$ defined in Eq. (105).

For a fiber element of normalized length λ, the quantity

$$H(\lambda, \tau, \pi(\cdot)) = \int_0^\lambda d\xi \left[\int_0^\tau (\pi(\xi, \zeta))^\rho d\zeta\right]^\beta \tag{43}$$

is called the *cumulative hazard* of fiber failure. Letting Z be an exponentially distributed random variable, i.e.,

$$\Pr\{Z \le z\} = 1 - \exp(-z), \tag{44}$$

the time to fiber failure has distribution given by Eq. (40) upon taking

$$Z \ge H(\lambda, \tau, \pi(\cdot)). \tag{45}$$

Stated otherwise, a fiber segment loaded (not necessarily uniformly) along its length breaks when its cumulative hazard exceeds its exponentially distributed, *standard representative random variable* Z. In the case of uniform loading, the cumulative hazard becomes

$$H(\lambda, \tau, \pi_u(\cdot)) = \lambda \left[\int_0^\tau (\pi_u(\zeta))^\rho d\zeta\right]^\beta$$

in terms of which Eq. (45) holds.

As a simple example we consider the constant load history

$$\pi_u(\tau) = \mathscr{R}, \quad \zeta \ge 0 \tag{46}$$

applied uniformly to a fiber of normalized length λ. Then its lifetime distribution normalized according to Eq. (41) is

$$\mathscr{F}_u(\tau) = 1 - \exp\left(-\lambda \mathscr{R}^{\rho\beta} \tau^\beta\right). \tag{47}$$

Another example from which an interesting interpretation of fiber "strength" emerges is the loading

$$\pi_u(\tau) = \mathscr{R}\tau, \quad \tau \ge 0 \tag{48}$$

linearly increasing in time with loading rate $\mathscr{R}$ and again uniform along the fiber. In terms of strength, $s = \mathscr{R}\tau$, and effective Weibull modulus, $\varrho = (\rho+1)\beta$, the distribution function for strength, Eq. (41), is

$$\mathscr{F}_u(s) = 1 - \exp\left(-\frac{\lambda}{(\rho+1)^\beta \mathscr{R}^\beta} s^\varrho\right). \tag{49}$$

Upon letting $\rho \uparrow \infty$ and $\beta \downarrow 0$ such that ϱ is fixed, then,

$$[(\rho+1)\mathscr{R}]^\beta = \frac{(\varrho\mathscr{R})^\beta}{\beta^\beta} \longrightarrow 1.$$

The strength becomes increasingly insensitive to loading rate.

4. Probabilistic Analysis of Composite Fracture

4.1. Equal Load Sharing Arrays

The simplest model is to assume a loose bundle of n fibers (no matrix and fibers held by clamps) loaded in tension. The load sharing in such a bundle is termed equal load sharing (ELS) whereby each failed fiber is unloaded along its full length, and when k fibers have failed, the stress concentration in each of the $n-k$ surviving fibers is

$$K_k = \frac{n}{n-k}. \tag{50}$$

Under the fiber model, Eq. (36), Phoenix (1978) has shown that the lifetime of an ELS bundle is asymptotically normally (Gaussian) distributed as $n \to \infty$. An important point is that for large ρ and intermediate n the derivation in Phoenix (1978) actually lends itself to obtaining an approximate log-normal lifetime distribution as was shown in Ibnabdeljalil and Phoenix (1995). This log-normal distribution transitions to asymptotic normal behavior as n becomes very large.

ELS is not expected to be valid for fibers embedded in a matrix since the matrix tends to concentrate redistributed stress on fibers near the breaks rather than equally redistributing it to fibers across the composite. Nevertheless, we will find that this tendency to normally distributed lifetime appears also for unit cells in large, local load-sharing bundles in which fiber breaking is highly dispersed, which in turn depends on the values of ρ, β and α and overall fiber volume nl.

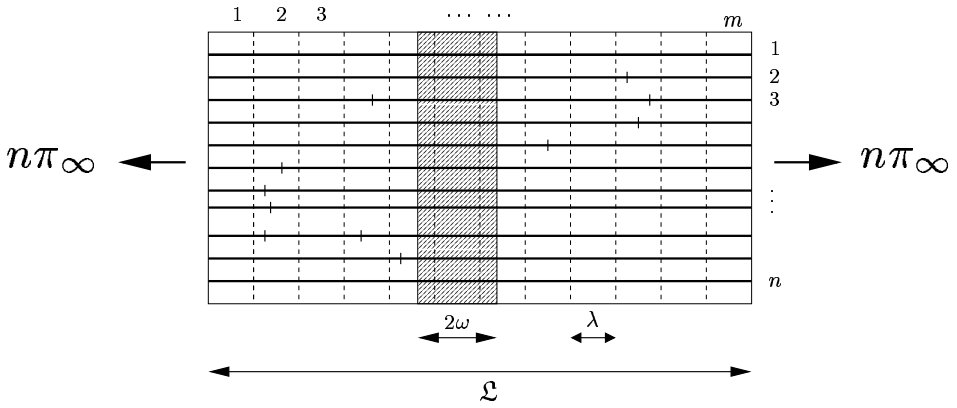

Figure 9. Chain-of-bundles subdivision of a composite of normalized length $\mathfrak{L}$ into m smaller λ-bundles each of whose failure is statistically and mechanically almost independent of the others. $\lambda = \mathfrak{L}/m$. 2ω is the longitudinal length scale of transverse load redistribution on fibers, which we will later take to be the overload length ahead of critical cluster of breaks (defined in Section 4.4).

4.2. Chain-of-Bundles Model

Composite failure typically corresponds to the formation of a transverse cluster or "crack" sufficiently large to become unstable. It is common to idealize the failure process in terms of a longitudinal partition of the composite of normalized length $\mathfrak{L}$ into a number, m, of transverse slabs or short bundles as shown in Figure 9, and to regard composite failure as the failure of the weakest such bundle (e.g., Smith (1980)).

Note that $\mathfrak{L}/m$ need not correspond to the longitudinal length scale of catastrophic transverse failure initiation in the composite. To see this let ω be the time-dependent stress overload length of a single break or a cluster of transverse breaks. Approximations for ω when fiber breaks are arranged transversely in 2D and 3D are given respectively in Eq. (23) and Eq. (26). Then 2ω and not $\mathfrak{L}/m$ (unless coincident) determines the longitudinal length scale of transverse stress redistribution. We will refer to each of the m bundles of real length λ and effective length 2ω as λ-bundles. Typically, $2\omega > \lambda$ and therefore, overload lengths of adjacent bundles may overlap causing their failure events to be dependent. This dependence, however, is only local owing to the relatively short range of the overload region. Thus many of the results of the fully independent case are excellent approximations. In particular, if $G_n(\tau)$ is the lifetime distribution of a single λ-bundle, and $H_{m,n}(\tau)$, that of the entire composite, then

$$H_{m,n}(\tau) \approx 1 - [1 - G_n(\tau)]^m. \tag{51}$$

4.3. Probability of k-Crack Formation

We now focus on modeling the failure of a single λ-bundle of n-fibers. First, we recognize the failure of k adjacent fibers in the λ-bundle as a likely precursor to the failure of the λ-bundle for any $k \leq n$, and call the event of its formation, k-cracking. Next let $Z_1, \ldots, Z_k$ be independent, unit exponentially distributed, standard representative random variables as described in Section 3. Let $T(Z_1, \ldots, Z_k; \lambda')$ be the normalized time required to fail a parallel arrangement of fiber elements where fiber i has standard representative random variable Z_i, for $1 \leq i \leq k$ and

$$\lambda' = \max(\lambda, 2\omega), \tag{52}$$

where 2ω is the longitudinal length scale of transverse cracking shown in Figure 9. Also let each fiber element be loaded in time such that the normalized load profile along its length is determined by two constants, $\mathfrak{K}$ and c, according to

$$\pi(\xi, \tau) = \pi_\infty \left[1 + (\mathfrak{K} - 1) \exp\left(-|\xi| c / \tau^{\alpha/2}\right)\right], \tag{53}$$

where $-\lambda'/2 \leq \xi \leq \lambda'/2$. Our notational distinction between $\mathfrak{K}$ and K is that K is thought of as the stress concentration ahead of a cluster of breaks, whereas $\mathfrak{K}$ more generally refers to that due to a set of arbitrarily located breaks. This choice of the functional form for $\pi(\xi, \tau)$ is motivated by the approximate stress profiles Eq. (24) and Eq. (28) in 2D and 3D respectively. $\mathfrak{K}$ and c may themselves be time-dependent quantities. The form Eq. (53) is chosen for the stress profile because it is a good approximation for the stress concentration ahead of a tight cluster of breaks, whose formation is the dominant mode of composite fracture under certain parametric conditions discussed shortly.

Configurations of fiber breaks other than a tight cluster may result in stress profiles considerably different from that of Eq. (53). We ignore such configurations (in the theoretical modeling but not in the Monte Carlo simulations) owing to their small probability of occurrence. Also the form Eq. (53), accurate for a cluster of breaks that form simultaneously may not be so good when breaks in the tight cluster form at widely different times. However we disregard these minor differences.

The general method is an adaptation of Tierney's (1980, 1982) to the load profile Eq. (53). The first scaling relation is independent of the far-field applied load π_∞, and for $\tau > 0$, is

$$\tau T(Z_1, \ldots, Z_n; \lambda') = T(\tau^{\beta+\alpha/2} Z_1, \ldots, \tau^{\beta+\alpha/2} Z_n; \lambda' \tau^{\alpha/2}) \tag{54}$$

or equivalently,

$$T(Z_1, \ldots, Z_n; \lambda') = \tau T(\tau^{-\beta-\alpha/2} Z_1, \ldots, \tau^{-\beta-\alpha/2} Z_n; \lambda'/\tau^{\alpha/2}). \tag{55}$$

This relation can be established inductively. When some l of the k fibers under consideration are broken (not necessarily as a tight cluster), let I be the set of $k-l$ fibers still intact and let $\mathfrak{K}_i(\tau)$ and $c_i(\tau)$ determine the stress concentration in fiber i, $i \in I$ according to Eq. (53). The variation of $\mathfrak{K}_i$ and c_i with time is mainly due to the formation of fiber breaks elsewhere in the bundle. Let $T_{l+1} \equiv T_{l+1}(Z_1, \ldots, Z_n; \lambda')$ be the time to failure of the next fiber. Then, for any $x > 0$, if $\mathfrak{K}_i > 1$, for $i \in I$, we can establish that

$$\begin{aligned} xT_{l+1} &\equiv xT_{l+1}(Z_1, \ldots, Z_n; \lambda') \\ &= \inf_{i \in I} \left\{ x\tau_i : Z_i \leq \int_0^{\lambda'} d\xi \left[\int_0^{\tau_i} [1 + (\mathfrak{K}_i - 1) e^{-\frac{\xi c_i}{\zeta^{\alpha/2}}}]^{\rho} d\zeta \right]^{\beta} \right\} \\ &= \inf_{i \in I} \left\{ \tau_i : x^{\beta} Z_i \leq \int_0^{\lambda'} d\xi \left[\int_0^{\tau_i} [1 + (\mathfrak{K}_i - 1) e^{-\frac{\xi c_i x^{\alpha/2}}{\zeta^{\alpha/2}}}]^{\rho} d\zeta \right]^{\beta} \right\} \\ &= \inf_{i \in I} \left\{ \tau_i : x^{\beta+\alpha/2} Z_i \leq \int_0^{\lambda' x^{\alpha/2}} d\xi \left[\int_0^{\tau_i} [1 + (\mathfrak{K}_i - 1) e^{-\frac{\xi c_i x^{\alpha/2}}{\zeta^{\alpha/2}}}]^{\rho} d\zeta \right]^{\beta} \right\} \\ &= T_{l+1}(x^{\beta+\alpha/2} Z_1, \ldots, x^{\beta+\alpha/2} Z_n; \lambda' x^{\alpha/2}) \end{aligned} \tag{56}$$

where intermediate steps involve appropriate changes of variables.

Similarly, a load scaling relationship can be established as follows. Let $T(Z_1, \ldots, Z_n; \lambda'; \pi_\infty)$ again be the time to failure but under external load π_∞. Then,

$$\begin{aligned} T(Z_1, \ldots, Z_n; \lambda'; \pi_\infty) &= T(Z_1/\pi_\infty^{\rho\beta}, \ldots, Z_n/\pi_\infty^{\rho\beta}; \lambda'; 1) \\ &= \pi_\infty^{-\frac{\rho\beta}{\beta+\alpha/2}} T(Z_1, \ldots, Z_n; \lambda' \pi_\infty^{\frac{\rho\beta\alpha/2}{\beta+\alpha/2}}; 1) \end{aligned} \tag{57}$$

where we have used Eq. (54) to obtain the second expression on the right hand side. Equivalently we have

$$\pi_\infty^{\frac{\rho\beta}{\beta+\alpha/2}} T(Z_1, \ldots, Z_n; \lambda'/\pi_\infty^{\frac{\rho\beta\alpha/2}{\beta+\alpha/2}}; \pi_\infty) = T(Z_1, \ldots, Z_n; \lambda'; 1). \tag{58}$$

Owing to their dependence on Eq. (54), the scaling laws, Eq. (57) and Eq. (58), also require that at each step $\mathfrak{K}_i > 1$, $i \in I$ in order to be valid. In the case that $\mathfrak{K}_i = 1$, for $i \in I$, (i.e., each successive break forms under the far-field load, being completely uninfluenced by any other break), we have the scaling relation

$$T(Z_1, \ldots, Z_n; \lambda'; \pi_\infty) = \pi_\infty^{-\rho} T(Z_1, \ldots, Z_n; \lambda'; 1). \tag{59}$$

In Section 6.1 we find that composites pass through an initial phase of dispersed fiber breaking under the far-field load wherein Eq. (59) is applicable. They then transition to a phase of clustered fiber failure wherein the form Eq. (53) with $\hat{\kappa}_i > 1$ is a good approximation for the stress concentration on fibers under risk of failure. Hence the actual scaling rule between load and lifetime can be expected to follow a load exponent between ρ and $\rho\beta/(\beta+\alpha/2)$, which will be seen in Section 6.1.

Letting $W_k(\tau)$ be the distribution function of $T(Z_1,\ldots,Z_k;\lambda';\pi_\infty)$, then we have

$$\begin{aligned}
W_k(\tau) &= \Pr\{T(Z_1,\ldots,Z_k;\lambda';\pi_\infty) \le \tau\} \\
&= \Pr\{\tau^{-1}\pi_\infty^{-\frac{\rho\beta}{\beta+\alpha/2}} T(Z_1,\ldots,Z_k;\lambda'\pi_\infty^{\frac{\rho\beta\,\alpha/2}{\beta+\alpha/2}};1) \le 1\} \\
&= \Pr\{T(\tau_1^{-\beta-\alpha/2}Z_1,\ldots,\tau_1^{-\beta-\alpha/2}Z_k;\lambda'/\tau^{\alpha/2};1) \le 1 \\
&= \int_{\mathbb{R}^k} 1_{[0,1]}(T(y_1,\ldots,y_k;\lambda'/\tau^{\alpha/2};1))\tau^{k(\beta+\alpha/2)}\pi_\infty^{k\rho\beta} \\
&\qquad \times \exp\left(-\tau^{\beta+\alpha/2}\sum_{i=1}^k y_i\right) dy_1\ldots dy_k \\
&\longrightarrow \lambda^*\{y\in\mathbb{R}_k^+ : T(y_1,\ldots,y_k;\lambda'/\tau^{\alpha/2}) \le 1\}\tau^{k(\beta+\alpha/2)}\pi_\infty^{k\rho\beta} \\
&\qquad \text{as } \tau\downarrow 0
\end{aligned} \tag{60}$$

by monotone convergence. In the step before the integral sign we let $\tau_1 = \tau\pi_\infty^{\frac{\rho\beta}{\beta+\alpha/2}}$ and used Eq. (55) and after the integral we set $y_i = \tau_1^{-\beta-\alpha/2}z_i$. Note also that λ^* denotes the Lebesgue measure (volume).

Tierney also provides an approximation for $\lambda^*\{y\in\mathbb{R}_k^+ : T(y_1,\ldots,y_k;\lambda'/\tau^{\alpha/2}) \le 1\}$ when ρ is large. Adapted to the load profile Eq. (53), it becomes,

$$\begin{aligned}
&\lambda^*\{y\in\mathbb{R}_k^+ : T(y_1,\ldots,y_k;\lambda'/\tau^{\alpha/2}) \le 1\} = \Gamma(1+\beta)^k\Gamma(k\beta+1)^{-1}\times \\
&\prod_{j=0}^{k-1}\left[2N_j\int_0^{\frac{\lambda'}{2\tau^{\alpha/2}}} d\xi\left\{\int_0^1 [1+(K_j(0)-1)\exp(-\xi c_j/\zeta^{\alpha/2})]^\rho d\zeta\right\}^\beta\right]
\end{aligned} \tag{61}$$

where we take $c_j = 1+1/\sqrt{j}$ for 2D arrays and $c_j = 2(1+1/\sqrt[4]{j})$ for 3D arrays, and N_j, the number of neighbors around a tight j-cluster, is

$$N_j = \begin{cases} 1, & \text{if } j = 0 \\ 2, & \text{if } j = 1,2,\ldots,k \end{cases} \tag{62}$$

in 2D and

$$N_j \approx \pi D = 2\sqrt{\pi j} \tag{63}$$

in 3D arrays. Here D is the tight j-cluster diameter determined by $\pi D^2/4 = j$. As detailed in Appendix B, Eq. (60) and Eq. (61) can be simplified when ρ is large to obtain

$$W_k(\tau) \approx (2\chi)^{k-1}\Gamma(1+\beta)^k\Gamma(1+k\beta)^{-1}\pi_\infty^{k\rho\beta}\tau^{k(\beta+\alpha/2)}\frac{\lambda}{\tau^{\alpha/2}}\prod_{j=1}^{k-1}\frac{N_j}{c_j}\frac{K_j^{\rho\beta+1}}{K_j-1}. \tag{64}$$

4.4. Critical k^*-Crack and Composite Lifetime

We let $G_n^{[k]}(\tau)$ be the probability of occurrence of at least one k-crack originating in a λ-long n-fiber bundle. Then following Tierney (1980, 1982) and Phoenix and Tierney(1983), we have

$$G_n^{[k]} \approx 1 - [1 - W_k(\tau)]^n. \tag{65}$$

Treating the composite as a serial arrangement of m such bundles, which are mechanically and statistically independent, the probability of occurrence of at least one k-crack in the composite, $H_{mn}^{[k]}(\tau)$, is

$$H_{mn}^{[k]}(\tau) \approx 1 - [1 - W_k(\tau)]^{mn}. \tag{66}$$

In cases where composite failure is ultimately driven by the formation and catastrophic propagation of a single dominant cluster of breaks (out of several that may initiate but lag the dominant one), composite failure may be regarded as a proper sub-event of the formation of a k-crack. Consequently, the distribution function for composite lifetime, $H_{mn}(\tau)$ may be bounded according to

$$\begin{aligned} H_{mn}(\tau) &\le \min_{1\le k\le n} H_{mn}^{[k]}(\tau) \\ &= \min_{1\le k\le n} 1 - [1 - W_k(\tau)]^{mn} \\ &= 1 - [1 - \min_{1\le k\le n} W_k(\tau)]^{mn} \\ &= 1 - [1 - W_{k^*}(\tau)]^{mn} \end{aligned} \tag{67}$$

where $k^*(\tau)$ is the crack size that minimizes $W_k(\tau)$ for each τ and is called the *critical cluster size*. In Section 6, when comparing to Monte Carlo simulations, we find the above upper bound to be especially tight when ρ is large so as to serve as a good approximation of the composite lifetime distribution function itself.

5. Monte Carlo Failure Simulation

5.1. Simulation Procedure

We now describe a Monte Carlo simulation model for the composite failure process, which has flaw arrangements roughly similar to but more general than the flaw geometry of the idealized unidirectional composite described in Section 1.1. The discretizations described below are essential to making the simulation algorithm reasonably fast. However, the extent of these idealizations is much smaller than those required in the construction of the subsequent analytical model.

Following the chain-of-bundles concept we conceptually partition the n-fiber 2D or 3D array of normalized length $\mathfrak{L}$ into m bundles, each of length $\lambda = \mathfrak{L}/m$. We will term the part of a fiber belonging to a bundle as a fiber *segment*. Each segment is further subdivided into $2f + 1$ ($\gg 1$) *fragments*. Thus there are m bundles, n fibers, mn fiber segments and $n_f = mn(2f + 1)$ fragments in the simulation cell. Fragment lengths are geometrically proportioned with the central fragment being the shortest and each fragment traveling away from the center longer than the previous fragment by a constant multiple. This is done to accommodate the sharper stress gradient that will tend to occur near the center. We denote the length of the i-th fragment by l_i, $i = 1, \ldots, n_f$. Each fragment is then assigned an independent standard representative random variable Z_i which is exponentially distributed with rate l_i. This is accomplished by producing uniform $U(0, 1)$ random variables $U_i, i = 1, \ldots, n_f$, from which $Z_i, i = 1, \ldots, n_f$, the desired standard representative random variables, are obtained according to

$$Z_i = -\frac{\log U_i}{l_i}, \quad i = 1, \ldots, n_f. \tag{68}$$

Failure of a fragment is assumed to occur at its mid-point.

Upon applying the far-field load π_∞ to the composite the first step is to determine the failure time τ_1 of the 'weakest' fragment, which by Eq. (41) is

$$\tau_1^\beta = \min_{i=1,\ldots,n_f} \frac{Z_i}{\pi_\infty^{\rho\beta}}. \tag{69}$$

Next the break location is transfered from the fragment where it occurs to the center of the associated segment. This simplification effectively renders the failure process more like the chain-of-bundles model of Section 4.2 than the idealized unidirectional composite of Section 1.1. However, this step is necessary for computational tractability, though we will shortly investigate its impact on the simulated composite lifetime distribution by varying λ. Fragments belonging to the fiber segment in

which the break occurs are then eliminated from future consideration by setting their Z_i's to ∞. This is done because the fragments within the broken segment are unloaded due to the break, and their failure probabilities become greatly reduced. Also, a subsequent break in the same segment will have minimal influence on the composite stress state.

Since every fiber break is transported to the mid-point of its associated segment, the peak overload on neighboring fibers occurs at the mid-points of the corresponding segments and decays roughly exponentially along the fibers down to the far-field value. For the purpose of determining the residual lifetime of a fragment in an overloaded segment, we assume constant stress along the fragment determined by value at its center. As mentioned, fragments closer to the segment mid-point are chosen to be shorter.

Successive segments are broken in a recursive manner. Let the stress concentration and the standard representative random number at the end of the $(k-1)$-th recursive step be $\mathfrak{K}_i(k-1)$ and $Z_i(k-1)$, $i = 1, 2, \ldots, n_f$ respectively. The k-th recursive step consists of determining the time to failure of the k-th break starting with a system of $k-1$ breaks and updating the quantities $\mathfrak{K}_i(k)$ and $Z_i(k)$ to reflect the presence of the new break. The k-th recursive step is begun by determining the smallest residual fragment lifetime using

$$\tau_{\rm res}(k-1) = \min_{i=i,..,n_f} \frac{Z_i^{\frac{1}{\beta}}(k-1)}{(\mathfrak{K}_i(k-1)\pi_\infty)^\rho}. \tag{70}$$

Global time is then advanced by $\tau_{\rm res}(k-1)$ and the time of the k-th fragment failure, $\tau_k = \tau_{k-1} + \tau_{\rm res}(k-1)$ is recorded. As before the break is then repositioned to the segment center. The standard representative random number of each surviving fragment is then updated as

$$Z_i(k) = Z_i(k-1) - (\mathfrak{K}_i'(k-1)\pi_\infty)^{\rho\beta}\tau_{\rm res}^\beta, \quad i = 1, 2, \ldots, n_f$$

to reflect the elapsing of time $\tau_{\rm res}$. Here $\mathfrak{K}_i'(k-1) = \max(\mathfrak{K}_i(k-1), 0)$. In order to speed up the computations, $\mathfrak{K}_i(k)$ is determined from shear-lag calculations only at segment centers and then is interpolated to fragment centers according to

$$\mathfrak{K}_i(\xi) = A + B\exp(-c\xi/\tau^{\alpha/2}), \tag{71}$$

where A and B are chosen so as to fit the stress concentrations determined by shear-lag calculations at segment centers. τ is taken to be τ_k, the time of formation of the k-th break. That is, interpolation assumes that all k breaks were formed at once at time 0. In keeping with Eq. (24) and Eq. (28) c is taken to be $1 + 1/\sqrt{k}$ in 2D and $2(1 + 1/\sqrt[4]{k})$ in 3D,

where k is the number of fiber breaks in the same bundle as the fiber segments between which interpolation is done. These steps are repeated until the failure criterion described in the next section is satisfied.

In the above recursion, the most time consuming operation by far is the computation of stress concentrations due to a set of breaks. It involves implementing the procedures of sections A.2 and A.3, and doing this efficiently is critical. Recall that as breaks are formed in succession, their weights are determined using Eq. (149). Then $[\Lambda(0^+)]_{(r\times r)}$ given a previous set of breaks is the northwest corner of the $[\Lambda(0^+)]_{(r+1\times r+1)}$ matrix with a new break appended to this set. It is imperative to exploit this structure to efficiently compute weights using Eq. (149). Since $-[\Lambda(0^+)]_{(r\times r)}$ is symmetric and positive definite, it permits Cholesky factorization of the form

$$-[\Lambda(0^+)]_{r\times r} = L_{r\times r}L^T_{r\times r} \tag{72}$$

where L is the lower triangular Cholesky factor (see Horn and Johnson (1985)). The solution for the weights is made efficient by storing, updating and using the Cholesky factor of the $-[\Lambda(0^+)]_{r\times r}$ matrix when stepping through fiber breaks. To update L to account for the formation of break $r+1$ in the presence of r breaks, we construct $B_{r\times 1}$ as the vector of influences of the previous r breaks on the $(r+1)$-th break. Then,

$$L_{(r+1)\times(r+1)} = \begin{bmatrix} L_{r\times r} & 0_{r\times 1} \\ X_{1\times r} & P_{1\times 1} \end{bmatrix} \tag{73}$$

where X is obtained by solving

$$L_{r\times r}X^T = B$$

by forward substitution and

$$P = \sqrt{1 - XX^T}.$$

We now now investigate the consequences of the key modeling difference between the present Monte Carlo simulation versus the more realistic description of the failure process in the unidirectional composite given in Section 1.1. In the above Monte Carlo model, flaws in effect occur in a uniform grid that passes through the centers of the m short fiber bundles. This has the effect of unrealistically aligning fiber breaks perpendicular to the fiber direction, and thereby, potentially facilitating the extension of break clusters since transversely aligned fiber breaks produce the greatest stress concentrations ahead of the cluster tip. Such a restriction is indispensable from a computation time standpoint since the determination of influences at possible break sites

in the uniform grid due to fiber breaks occurring at other sites in the uniform grid can be done by translating the influences of a single break anywhere in the grid according to Eq. (143) and Eq. (144). On the other hand, if the potential break sites were situated arbitrarily, the entire influence field of each fiber break on all other potential break sites would have to be recalculated using the shear lag methodology. Alternatively stresses could be interpolated from a regular grid to the locations of arbitrarily occurring break sites, but this approach is unsatisfactory because stresses can vary exponentially in the array.

As it turns out, alignment of fiber breaks in the Monte-Carlo model is not much of an issue when the length of a segment λ is much smaller than the overload length ahead of the cluster tip. Indeed, it would be best to choose λ as small as possible in order to reduce the effects of such alignment. In our simulations, we have found it satisfactory to take $\lambda = 0.5$, which is near the practical limit of our our computational capability. We divide each λ into $n_f = 11$ fragments.

We have simulated the failure of 2D and 3D arrays of $n = 100$ fibers of normalized length $\mathfrak{L} = L/\delta_{\mathrm{v}} = 10$ under periodic boundary conditions. To determine fiber statistics through Eq. (41), we have considered three combinations of (β, ρ), namely $(0.1, 75)$, $(0.3, 25)$, and $(0.5, 15)$. In all cases, we have $\rho \gg 2$, which far exceeds the transition to percolation breakdown calculated by Curtin and Scher (1997) and Newman and Phoenix (2001). The role of matrix viscoelasticity was studied by considering three powers for the power law compliance, namely $\alpha = 0$, 0.1 and 0.5, where $\alpha = 0$ corresponds to the elastic case. Failure was also studied under three different applied loads, namely $\pi_\infty = 0.3$, 0.5 and 0.7. For each set of parameter values we tested $n_{\mathrm{sim}} = 1024$ virtual composite specimens. The simulations were performed on a cluster parallel computer of Intel 500 MHz processors. Depending on the parameters of the model, computations took anywhere between 0.5 and 1500 processor-hours.

5.2. Determining the Time of Composite Failure

A crucial aspect is to establish the critical event that signals composite failure in the simulation algorithm above. We consider three reasonable possibilities. The first is that failure is taken to occur when the composite strain rate ($\dot{\varepsilon}$) exceeds a fixed threshold, $\dot{\varepsilon} > \varepsilon_{\mathrm{c}}$. Composite strain is easily determined from the sum of fiber break opening displacements, which are the weights $w(\tau)$ in Eq. (149). A second approach is to consider the composite failed if a bundle of some appropriately chosen length (say the characteristic length or overload length for some fixed k) has all fibers in it failed. Here k must be chosen large enough to

represent a critical cluster, i.e., one which will continue to propagate with almost certainty. A third approach of a purely numerical nature is to identify composite failure with the sudden acceleration of occurrence of successive fiber breaks by considering the composite failed if

$$\frac{\tau_{i+1} - \tau_i}{\tau_{i+1}} < \epsilon \tag{74}$$

where τ_i is the time of formation of the i-th break and ϵ is a suitably chosen small constant.

We use this third approach, taking Eq. (74) as our failure criterion with ϵ taken to be the computer's machine precision (about 10^{-16}). From a set of benchmark simulations that exercised the entire parameter range of our failure simulations, we found the criterion given by Eq. (74) to be the most conservative of the three criteria in that its satisfaction occurs only after the satisfaction of the other two. The first two, however, have a mechanical basis, while the third does not though it is based on the observation that the time between successive fiber failures becomes progressively small after the composite goes unstable. Consequently, the satisfaction of the first two criteria (which occur more or less at the same time) signal composite instability and the continued simulation up to the satisfaction of the third criterion could result in significant post-critical fiber breaking often removed from the cluster of breaks that became unstable. These post-critical breaks, however, are of no concern since they are formed well after the failure process in the composite has gone catastrophic and they actually take negligible time to form, thereby hardly affecting the simulated empirical lifetime distribution.

5.3. Failure Configurations and Modes

Depending on the fiber and matrix parameter values and the applied composite load π_∞, composite failure is dominated by one of two qualitatively distinct modes of failure: (i) a clustered failure mode, which accompanies high fiber failure sensitivity to load level, high applied load and short overload length, or, (ii) a dispersed and more global failure mode, which accompanies relatively lower fiber failure sensitivity to load level, small applied loads and longer overload lengths. In a later section, distinctly different theories will be required to model the lifetime distributions for these two modes.

For the clustered failure mode, (i), Figure 10 shows the arrangement of fiber failures in the vicinity of the composite failure plane in the median specimen among $n_{\text{sim}} = 1024$ simulations of $n = 100$ fiber, $\beta = 0.1$, $\rho = 75$, $\alpha = 0$ (elastic matrix) composite under applied load

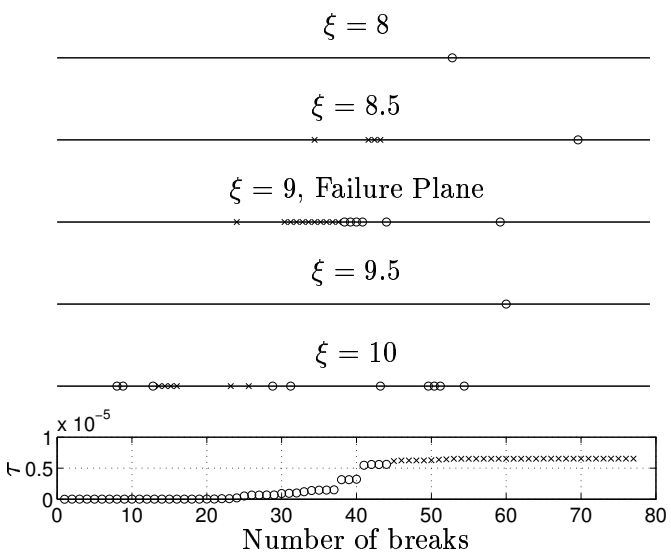

Figure 10. Snapshot of damage near the failure plane in the median $\beta = 0.1$, $\rho = 75$, $\alpha = 0$ specimen (elastic matrix) among $n_{\text{sim}} = 1024$ simulations under applied load $\pi_\infty = 0.7$ and at time $\tau = 6.536 \times 10^{-6}$ when the failure criterion Eq. (74) is satisfied by the formation of 77 fiber breaks out of a possible 2,000. Each horizontal line spans a bundle of $n = 100$ fibers and successive bundle centers are spaced $\lambda = 0.5$ apart. Only five out of the twenty bundles in the simulation cell are shown. Each $\circ$ denotes a fiber broken before the composite goes unstable according to the strain criterion (which is satisfied after the formation of 44 fiber breaks) and each $\times$ denotes a post-critical broken fiber. Notice that the critical cluster size $k^* = 4$ and that staggering of breaks in the catastrophic cluster occurs between planes $\xi = 8.5$ and $\xi = 9$. The box at the figure bottom plots the times when fiber breaks occur.

$\pi_\infty = 0.7$. Longitudinally this composite is divided into $m = 20$ bundles and the normalized length of each segment is $\lambda = 0.5$. Figure 11 shows the evolution of composite strain over time for this same specimen. The strain grows catastrophically after the failure of 44 fiber segments at time $\tau_{44} = 0.5615 \times 10^{-5}$. As Figure 10 shows, however, after 44 breaks the incremental times between fiber failures become negligible in sum suggesting that this particular specimen goes unstable after just 44 fiber breaks have formed. The number of contiguous fiber breaks in the final failure plane at the time when propagation rapidly accelerates is only $k^* = 4$. We return to this observation in Section 6.

The clustered failure mode, (i), decreases in prominence and sharpness when ρ decreases. This is in qualitative accord with Eq. (41) since it diminishes the rate of increase of the probability of fiber segment failure. The transition from a clustered to dispersed failure mode is signaled by increased out-of-plane fiber failures ahead of the cluster

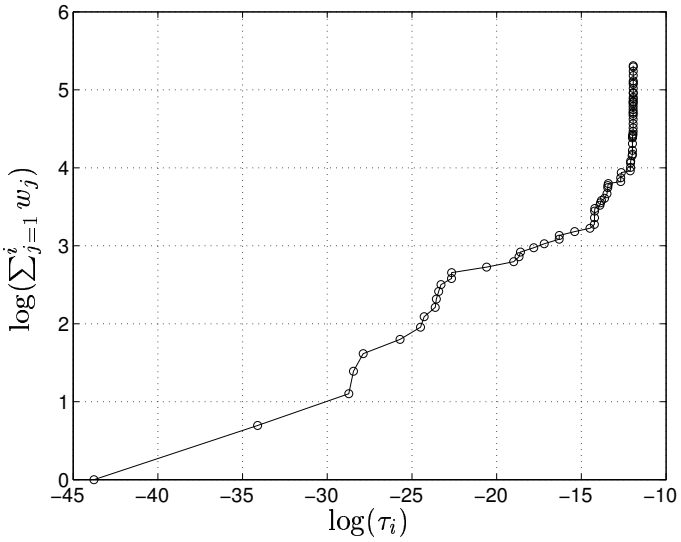

Figure 11. Plot of strain versus time in the median $\beta = 0.1$, $\rho = 75$, $\alpha = 0$ (elastic), specimen under applied load $\pi_\infty = 0.7$. Each $\circ$ denotes the time of formation of a fiber break. Initially the strain grows moderately as breaks accumulate randomly in the composite, but then a cluster forms and extends more quickly. The cluster growth goes critical, causing cluster extension to proceed rapidly prompting the blow-up of composite strain starting at break number 45.

tip. Note that both the terms – "clustered" and "dispersed" – refer to parameter value sets that still lie in the "avalanche" regime of Curtin and Scher (1997). We do not consider parameter sets in their "percolation" regime, nor do we investigate parameter values for a transition to such a region.

Figures 12, and 13 correspond to a case wherein out of plane break staggering is prevalent although the composite still fails by the formation of a cluster of breaks spanning several transverse planes (bundles). Figure 12 shows the evolution of strain with time in the median among $n_{\text{sim}} = 1024$ specimen of $\beta = 0.5$, $\rho = 15$ and $\alpha = 0$ (elastic matrix) composites under applied load $\pi_\infty = 0.3$. In contrast to Figure 11, strain increments occur rather continuously owing to the large number of initial dispersed breaks that form, seemingly in an uncorrelated manner, before a growing cluster is initiated. While no sharp point is clearly identifiable signaling the start of strain blow-up, we take this number to be 101 breaks, where the strain rate (not shown) shows a first large acceleration. We show the configuration of fiber breaks at that time in Figure 13, where a cluster of breaks forms that straddles planes $\xi = 8$ to $\xi = 9.5$ and frequently switches between planes.

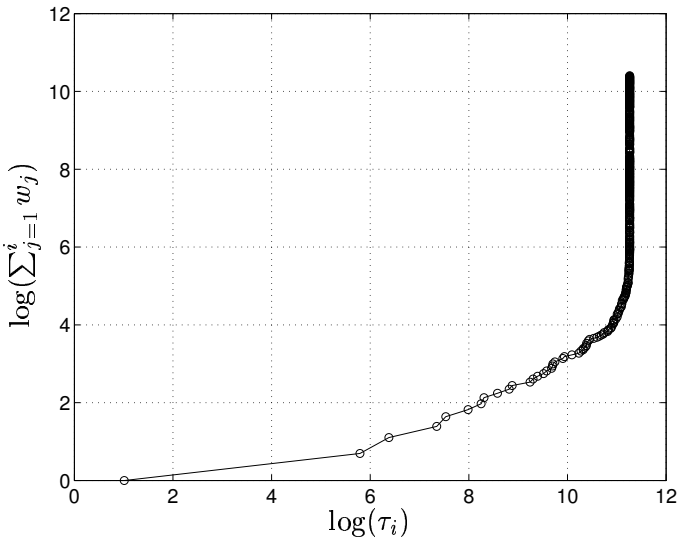

Figure 12. Plot of strain versus time in the median $\beta = 0.5$, $\rho = 15$, $\alpha = 0$, under applied load $\pi_\infty = 0.3$. Each $\circ$ denotes the formation of a new break. Dispersed initial breaks take up much of the lifetime of this composite with criticality apparently reached when the dispersed failures have reached a certain concentration. This happens in this specimen when the number of breaks is 94.

At the opposite end of the spectrum we have composites that appear to fail by a dispersed fiber failure almost entirely up to instability, i.e., mode (ii) above. By continuing simulations well past the onset of strain instability we still induce large cluster formation, as this represents eventual localization but a more global-like load sharing system occurs up to that point. Figure 14 shows the break configuration in the entire composite with $\beta = 0.5$, $\rho = 15$ and $\alpha = 0.5$ (a strongly viscoelastic matrix) at applied load $\pi_\infty = 0.3$. The strain instability criterion is satisfied when almost the entire lifetime of the composite has elapsed. The difference between this and the previous much more localized cases lies in the length of the overload zone. In Figure 13, since the matrix was elastic, the overload zone was confined to its time independent value of approximately $2\delta_v$. In Figure 14, however, the overload zone eventually expands to cover almost the total length of the composite cell, increasing many-fold the opportunity for staggering of a crack. This increasingly becomes an issue as α increases further. Another important point is that since normalized time τ spans many decades, the overload length $\omega \propto \tau^{\alpha/2}$ varies considerably. Since staggered clusters or cracks propagate with lower probabilities than aligned cracks, owing to

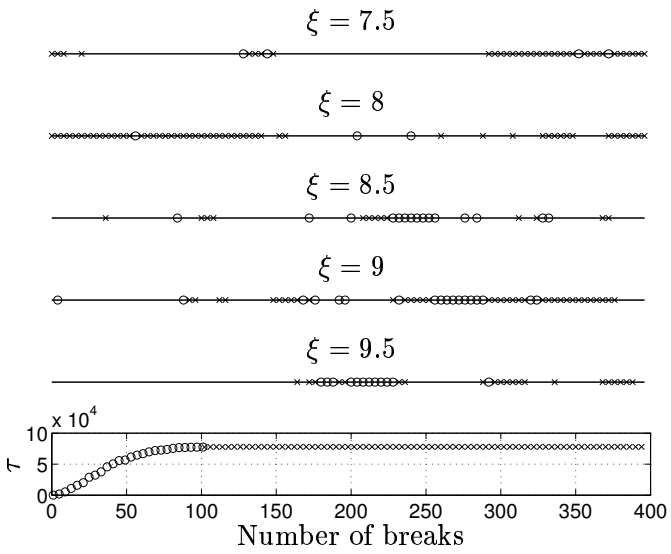

Figure 13. Snapshot of the damage near the failure volume of a median $\beta = 0.5$, $\rho = 15$, $\alpha = 0$, specimen among $n_{\text{sim}} = 1024$ under applied load $\pi_\infty = 0.3$, at $\tau = 7.788 \times 10^4$ when the failure criterion Eq. (74) is satisfied. The meanings of the horizontal line, $\circ$, and $\times$ are identical to those in Figure 10. Notice the extensive stagger between bundles centered at $\xi = 8.5$, $\xi = 9$ and $\xi = 9.5$. The failure plane is not identifiable; instead the bundles centered about these three planes maybe be thought as a failure volume. After the critical cluster has formed, failure progresses in the plane $\xi = 8$ to a larger extent. The bottom box shows the times of formation of breaks, where only every fourth break has been marked for legibility.

the smaller stress concentrations ahead of them, this favors the general propensity toward dispersed fiber breaking.

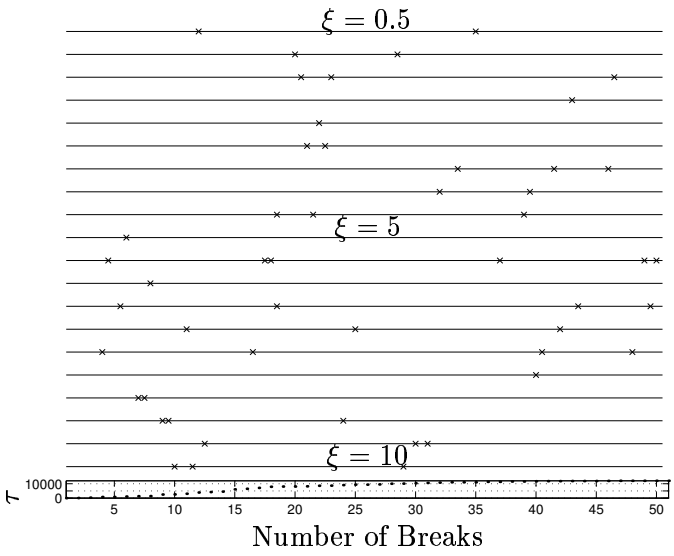

Figure 14. Completely dispersed failure snapshot of the median $\beta = 0.5$, $\rho = 15$, $\alpha = 0.5$, composite under applied load $\pi_\infty = 0.3$, at time $\tau = 1.21 \times 10^4$ when it goes critical as per the strain criterion. The overload length of a single break at this time almost encompasses the whole of the composite.

6. Comparison of Monte Carlo Empirical and Analytical Lifetime Distributions

In this section, we compare the empirical lifetime distributions obtained from the Monte Carlo simulations described in Section 5 and the analytical model developed in Section 4. The gradual transition from a localized failure mode, (i) to a global failure mode, (ii), as seen in the failure patterns of Section 5.3 is reflected in their lifetime distributions changing from a weakest-link form with a characteristic distribution function in the cluster formation and growth case, to a log-normal or normal distribution in the dispersed failure case. Since computational limitations necessitate a small size for the simulated unit cell, we must pay particular attention to the role of boundary effects (here manifested as the effects of periodic boundary conditions) on the composite failure and will find that periodic boundary conditions impel composites (cells) that are too small toward a dispersed failure mode.

Empirical distributions discussed are those of $n = 100$ fiber composites of normalized length $\mathfrak{L} = 10$ divided into $m = 20$ bundles longitudinally. According to this division in each fiber there are two fiber segments per characteristic length δ_v. Therefore, the empirical weakest link distribution $\hat{W}(\tau)$ is derived from the empirical composite

lifetime distribution $\hat{H}_{mn}(\tau)$ according to

$$\hat{W}(\tau) = 1 - (1 - \hat{H}_{mn}(\tau))^{1/mn} \tag{75}$$

where $mn = 20 \times 100 = 2,000$ in the remainder of this discussion (i.e., the total number of fiber segments is $2,000$).

6.1. 2D Arrays

6.1.1. *Lifetime Distribution*

A key quantity affecting the lifetime distribution function $H_{mn}(\tau)$ is the stress concentration ahead of a cluster of k fiber breaks. As seen in the failure configurations of Section 5.3, the typical propagating cluster of k breaks tends to be somewhat staggered. In view of this fact and our observations in Section 2.2 regarding the effect of periodic boundary conditions and staggering ahead of a cluster of k breaks in Eq. (29) and Eq. (31), respectively, we take the form of the stress concentration ahead of a cluster of k breaks in 2D arrays to be

$$K_k(\tau) = \sqrt{\frac{\pi k}{8}\psi_k(1 - \exp(-\mathfrak{L}/(k\tau^{\alpha/2}))) + 1} \tag{76}$$

where we provisionally let ψ_k be a free parameter. In Eq. (76), the factor $1 - \exp(-\mathfrak{L}/(k\tau^{\alpha/2}))$ comes from Eq. (29) and is a correction for the periodicity of the composite patch along the fiber direction. As seen in Section 5.3, staggered k-clusters of breaks hardly ever occur in pairs of $(k/2)$-clusters as idealized in Eq. (31); the number of cluster limbs may exceed two, and their relative size is random. Eq. (31) is thus unrealistically specialized to be a good model of load concentration ahead of a staggered cluster of breaks. Therefore, we approximately account for cluster staggering using the parameter ψ_k in Eq. (76), and drop the correction ψ_1 which appears in Eq. (31). The utility of Eq. (31) lies in showing where this correction is to be applied: as a multiplier of $\pi k/8$.

The dependence of $K_k(\tau)$ on τ is weak and τ may be varied considerably without significantly affecting $K_k(\tau)$. We therefore can let τ in Eq. (76) be the normalized time since the formation of the first break in the k-cluster without affecting the approximation much.

In addition to accounting for the influence of interaction between periodic unit cells, this form for K_k also accounts for the staggering of fiber breaks through the parameter ψ_k. It suffices to let

$$\psi_k = \begin{cases} 1 & \text{if } k < k_0 \\ \psi & \text{if } k \geq k_0 \end{cases} \tag{77}$$

where k_0 is appropriately chosen and ψ is maintained as a free parameter, which is chosen so as to produce the tightest bound in the lower tail of the simulated empirical lifetime distributions. We only allow $1 \leq \psi \leq 2$, where $\psi = 1$ corresponds to the k-cluster being comprised of two equal limbs (as defined before Eq. (31)) infinitely apart while $\psi = 2$ corresponds to the case where the two limbs are aligned transversely.

The form Eq. (76) with the restriction Eq. (77) at best represents an attempt to capture the dominant effect of the stress concentration ahead of a staggered cluster of k-breaks using the fewest fitting parameters. The chosen form results in predicted lifetime distributions that accurately capture the form of the empirical distributions.

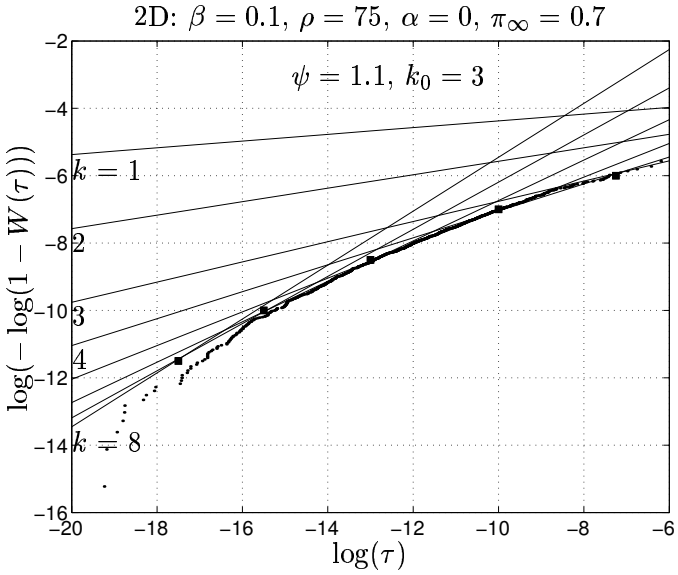

Figure 15. Comparison of the empirical weakest link distribution with the k-envelope given by Eq. (64) in a $\beta = 0.1$, $\rho = 75$ and $\alpha = 0$ (elastic matrix) composite on Weibull coordinates under applied load $\sigma = 0.7$. To get good agreement, we chose $\psi = 1.1$ and $k_0 = 3$. Points of intersection of the k-lines are marked with squares.

Figure 15 shows the comparison between the empirical $\hat{W}(\tau)$ obtained from Monte Carlo simulations and $W_k(\tau)$, $k = 1, \ldots, 8$, from Eq. (150) for the case of a composite under applied load $\pi_\infty = 0.7$ wherein the matrix is elastic $\alpha = 0$ and fiber statistics are determined by the parameters $\beta = 0.1$ and $\rho = 75$. According to Eq. (67), the model predicts an upper bound that is the minimum envelope of the shown $W_k(\tau)$. To obtain good agreement between $\min_k W_k(\tau)$ and $\hat{W}(\tau)$, we have set the free parameters as $\psi = 1.1$ and $k_0 = 3$. The

minimum envelope of $W_k(\tau)$ approximates the shape of $\hat{W}(\tau)$ well, but divergence is seen in the lower tail. Decreasing ψ for larger k would reduce this divergence. Doing so is physically justifiable since larger k corresponds to increased staggering, which can be corrected for by making ψ smaller. The empirical median lifetime of this composite is found to be $\tau_{1/2} \approx 6.5 \times 10^{-6}$ at which time $k^* = 4$ in the Weibull lower envelope. From Figure 10 it can be seen that the critical cluster size k^* in the failure plane of the median specimen is indeed 4.

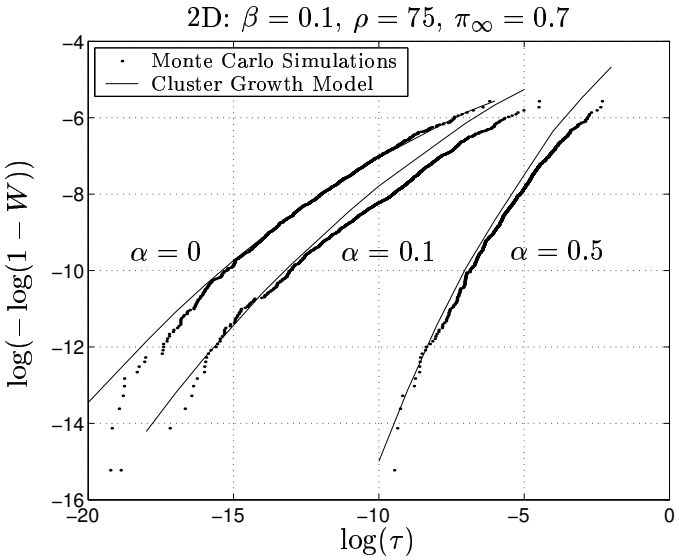

Figure 16. Comparison on Weibull paper of the empirical weakest link distribution with the minimum of the k-envelope in $\beta = 0.1$, $\rho = 75$ fiber composites with matrix of three different α: $\alpha = 0$, 0.1, and 0.5 under stress $\pi_\infty = 0.7$. The (ψ, k_0) pairs for these three α are respectively, $(1.1, 3)$, $(1.4, 3)$ and $(1.75, 3)$.

Figure 16 shows the Weibull lower envelope for composites where $\beta = 0.1$, $\rho = 75$ and $\alpha = 0$, 0.1 and 0.5, the first of which was just discussed. The applied normalized load is $\pi_\infty = 0.7$. The median lifetimes of the three cases varies in the reverse order of their overload lengths ω_k at the failure time. The median lifetimes of the $\alpha = 0$, $\alpha = 0.1$, and $\alpha = 0.5$ composites are, respectively, $\tau_{1/2} = 6.5 \times 10^{-6}$, 7.7×10^{-6} and 6.0×10^{-3}. In all three cases, the median lies in the range of $k^* = 4$. This implies that the approximate normalized overload lengths calculated using Eq. (23)are $\check{\omega}_4 = 2$, 1.11, and 0.56 respectively. Since the elastic ($\alpha = 0$) composite has an overload zone next to a fiber break, which instantaneously extends to $\omega_4 = 2$, a break in it subjects a greater length of its neighboring segment to overload than it would in an $\alpha = 0.1$ or $\alpha = 0.5$ viscoelastic composite. This qualitatively

explains the observed trend in the median lifetime. In computing the model lines for the three different cases, we have substituted $\tau = \tau_{1/2}$ in Eq. (76) without appreciable error. While $k_0 = 3$ is fixed in all three cases, $\psi = 1.1$, 1.4, and 1.75 when $\alpha = 0$, 0.1, and 0.5 respectively. This is in keeping with the overload length argument suggested above; correction necessary to account for staggering is smaller if the overload length is shorter. This in turn results in ψ closer to 2 as α increases.

The disagreement in the lower tail between the predicted and empirical weakest-link distributions, seen previously for $\alpha = 0$, decreases and almost disappears as α is increased up to 0.5. Viewed in conjunction with the increased possibility of staggering that accompanies increased overload length ω_k as α decreases according to $\omega_k \propto \tau^{\alpha/2}$, this bolsters our earlier suggestion that the assumed forms Eq. (76) and Eq. (77) for K_k are imperfect and break down as fiber break staggering ahead of a cluster becomes pronounced.

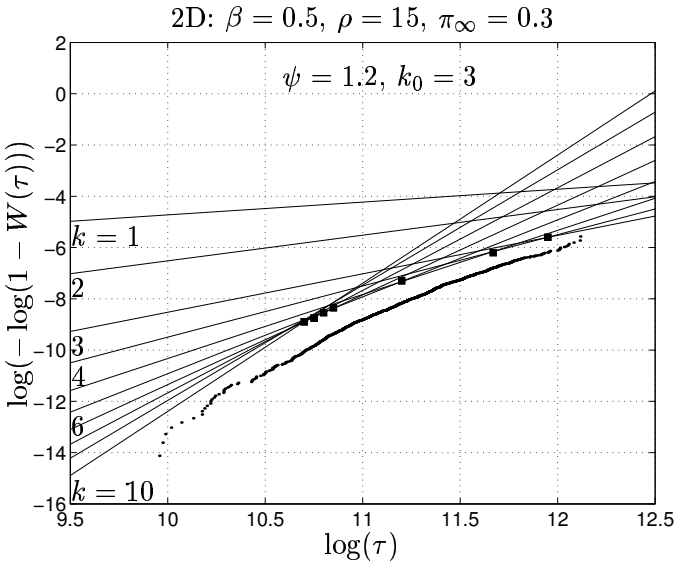

Figure 17. Inability of the k-envelope model to fit the empirical weakest-link distribution for composites with $\beta = 0.5$, $\rho = 15$ and $\alpha = 0$ (elastic matrix) under load $\pi_\infty = 0.7$. Lines for $k > 5$ appear to intersect (as marked with squares)almost at a single point. For the other parameters we have taken $\psi = 1.2$ and $k_0 = 3$.

As indicated earlier, the cluster growth failure mode, (i), gives way to a dispersed failure mode, (ii), as cluster extension probability is decreased. In Figure 17, in attempting to fit $W_k(\tau)$ to the weak-linked, lifetime distribution of an elastic matrix composite ($\alpha = 0$) with fiber parameters $\beta = 0.5$ and $\rho = 15$, we find that the lines of $W_k(\tau)$ intersect each other almost at one point when k exceeds about 5. An explanation

follows from the boundedness of stress concentrations ahead of a k-cluster of breaks in a unit cell under periodic boundary conditions in accordance with Eq. (29). Let K_L be this upper bound for a unit cell of length $\mathfrak{L}$. That is, let $K_{k,L} < K_L$, for $k = 1, 2, \ldots$. Then for sufficiently large k, the ratio W_{k+1}/W_k becomes

$$\begin{aligned}\frac{W_{k+1}(\tau)}{W_k(\tau)} &= \frac{2\chi\Gamma(1+\beta)}{c_k}\frac{\Gamma(1+(k+1)\beta)}{\Gamma(1+k\beta)}\left(1-\frac{1}{K_{k,L}}\right)^{-1}(K_{k,L}\pi_\infty)^{\rho\beta}\tau^{\beta+\alpha/2} \\ &\approx 2\chi\Gamma(1+\beta)\beta^\beta\gamma(k)(K_L\pi_\infty)^{\rho\beta}\tau^{\beta+\alpha/2}\end{aligned} \tag{78}$$

where $\gamma(k) = O((k+1)^\beta)$ is a slowly increasing function of k when β is small. From this we may define an *accumulation time*

$$\tau_{\mathrm{a}} = (2\chi\Gamma(1+\beta)\beta^\beta\gamma(k)(K_L\pi_\infty)^{\rho\beta})^{-\frac{2}{\alpha+2\beta}}. \tag{79}$$

whereby $W_{k+1}(\tau) < W_k(\tau)$, for $\tau < \tau_{\mathrm{a}}$ and all $k > k_0$ for some k_0. For $\tau \geq \tau_{\mathrm{a}}$, however, there is a unique k^* such that $W_{k^*}(\tau) \leq W_k(\tau)$, for all k where $k^* = k^*(\tau)$. By this argument, accumulation of W_k of the above described nature should occur for all values of β and ρ for sufficiently high k in a composite cell.

Once the stress concentration ahead of a cluster of breaks does not substantially increase with further increases in cluster size, cluster extension must proceed at the same speed irrespective of cluster length. In this condition a global damage mode appears to take over and fibers fail in a dispersed manner until they link up and fail the composite.

Dispersed failure is characteristic of equal load-sharing bundles, which have Gaussian (normal) lifetime distributions asymptotically as $n \to \infty$, as discussed in Section 4.1. That gives us reason to expect the same distribution even in local load sharing composites when fiber failure is also dispersed. However, we do not find obvious normal tendencies for any of our simulated lifetime distributions. A second possibility (Curtin (1998)), suggested by the longitudinal localization of dispersed fiber breaks within bands smaller than the composite length, is that the empirical lifetime distribution follows

$$\hat{H}_{mn}(\tau) \approx 1 - (1 - \hat{W}(\tau))^{\hat{m}} \tag{80}$$

where $\hat{W}(\tau)$ is approximately Gaussian and the composite may be thought of as a weakest link arrangement of $\hat{m}$ equal load-sharing bundles. However again, $\hat{W}(\tau)$ determined from Eq. (80) fails to be Gaussian for any $\hat{m}$ as determined from our simulation $\hat{H}_{mn}$ data.

It turns out, however, that $\hat{W}(\tau)$ is very linear on log-normal coordinates which differs from the normal coordinates in that the horizontal

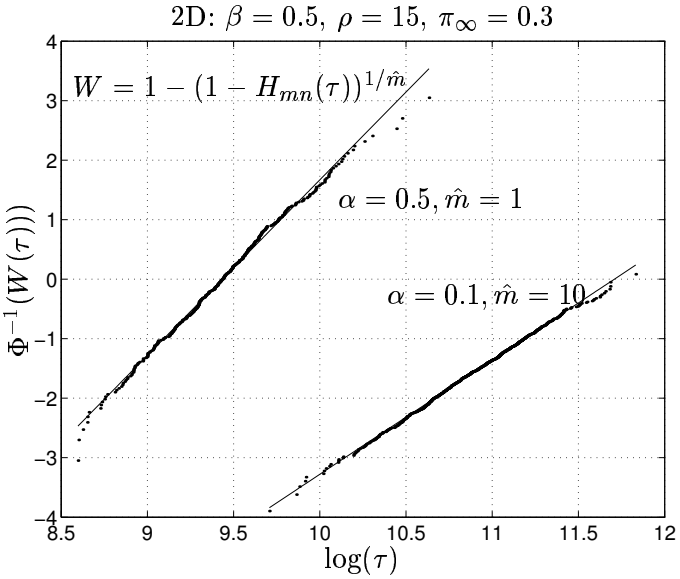

Figure 18. Plots of the weak linked empirical distribution of $\beta = 0.5$, $\rho = 15$ composites under applied stress $\pi_\infty = 0.3$ on log-normal paper. The linearity of the plots suggests that the weak linked distributions are log-normal.

axis is $\log \tau$ instead of τ. Figure 18 shows the weak-linked lifetime distributions of $\beta = 0.5$, $\rho = 15$ composite specimens with matrix creep exponents of $\alpha = 0.1$ and $\alpha = 0.5$ on log-normal probability coordinates together with straight lines which are least squares fits of them. Here $\hat{m}$ is chosen in each case to be the integer which minimizes the standard error of both the slope and intercept estimates of the fitting straight lines. The line corresponding to $\alpha = 0$ is excluded from this figure since the standard error corresponding to it does not achieve a minimum at any reasonable $\hat{m}$ and continually decreases as $\hat{m}$ is increased and the concept fails to work, i.e., the form Eq. (80) does not capture the distribution of $\hat{H}_{mn}$ for $\alpha = 0$. This observation is in agreement with Figure 17 which shows that the k-cluster growth model is a reasonable assumption until it is superseded by non-accelerating crack growth due to the influence of its periodic images. Thus the case $\alpha = 0$ behaviorally appears to lie between the clustered and dispersed failure modes for this limited unit cell size.

We use reasoning found in Ibnabdeljalil and Phoenix (1995) to explain the observed log-normal nature of the link $W(\tau)$ of $H_{m,n}(\tau)$. It hinges on the connection between the lifetime problem and the static strength problem established through Eq. (49). Monte Carlo simulations show that the strength of equal load-sharing bundles converges

rapidly in distribution to the normal distribution even when the bundles are as small as $n = 5$. This is in contrast to the lifetime of equal load-sharing bundles whose convergence in distribution to a normal distribution is much slower, so that the convergence is not nearly complete even for $n = 500$. Since our weakest link bundles are quite small, their lifetime distribution is non-normal in shape.

To see how log-normality arises we must determine the lifetime distribution that corresponds to a given normal strength distribution. Following Ibnabdeljalil and Phoenix (1995) and Phoenix (1978) the standardized lifetime of an equal load sharing bundle has the scaling

$$\mathscr{T} = \begin{cases} \int_0^T \pi^\rho(s)ds = T\pi_\infty^\rho, & \text{if } \pi(s) = \pi_\infty \\ \int_0^{T'} \pi^\rho(s)ds = \frac{\mathscr{R}^\rho T'}{\rho+1}, & \text{if } \pi(s) = \mathscr{R}s \end{cases} \tag{81}$$

where T and T' are the actual failure times under the two kinds of loadings – constant and linearly increasing, and where $\mathscr{R}$ is the loading rate and $\mathscr{T}$ is a standard time assuming $\pi_\infty = 1$. This remarkable result for both the fiber and the bundle emerges from the factorization property of the power law breakdown rule in integrals (Phoenix (1978)). Equating the two right hand sides and substituting the strength-time relationship $\Sigma = \mathscr{R}T'$ in the linearly increasing load case gives

$$T\pi_\infty^\rho = \frac{\mathscr{R}^\rho T'}{\rho+1} = \frac{\Sigma^{\rho+1}}{(\rho+1)\mathscr{R}} \tag{82}$$

which implies that

$$\Sigma \propto \mathscr{T}^{\frac{1}{\rho+1}} \approx \frac{1}{\rho+1}\log(\mathscr{T}) + 1 \tag{83}$$

where the latter approximation is accurate for large ρ ($\rho \geq 10$, say) and $\mathscr{T}$ close to one. Since Σ is normal, this suggests that $\mathscr{T}$ must be very close to log-normal.

6.1.2. *Important Scaling Relations*

Within a bundle wherein each fiber is subjected to the stress concentration based load profile of Eq. (53), a scaling relation between the applied load and lifetime was derived in Eq. (57). In the absence of fiber stress concentrations the scaling relation was found to be Eq. (59). The actual stress state in a partially failed composite lies between these extremes and we now consider the actual scaling relationship seen in our Monte-Carlo simulations.

Figure 19 shows the variation of the median composite lifetime, $\tau_{1/2}$, with applied bundle load, π_∞, for $\beta = 0.1$ and $\rho = 75$ for the fiber and $\alpha = 0$, 0.1, and 0.5 for the matrix. When $\alpha = 0$, the load-lifetime

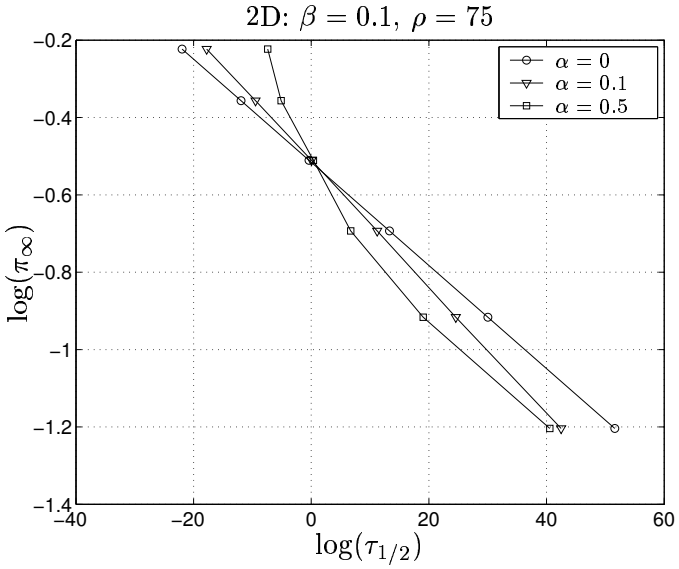

Figure 19. Scaling of the median lifetime($\tau_{1/2}$) with applied load(π_∞) for Monte-Carlo simulated composites with $\beta = 0.1$, and $\rho = 75$ and different α. In the case of the elastic matrix, $\alpha = 0$, the scaling relation is $\pi_\infty^{75}\tau_{1/2} = c$ exactly where c is a constant. When $\alpha = 0.1$, the scaling $\pi_\infty^{58}\tau_{1/2} = c$ is a good approximation. When $\alpha = 0.5$, a simple power law scaling fails to hold.

scaling relation Eq. (57) collapses into Eq. (59) which appears to hold in the simulations. Thus, the median lifetime $\tau_{1/2}$ scales exactly as $\pi_\infty^{-\rho}$. However when $\alpha > 0$, the behavior is more complicated. While Eq. (57) suggests the form $\pi_\infty^{\rho\beta/(\beta+\alpha/2)}\tau_{1/2} =$ constant for the load-lifetime scaling, which for $\alpha = 0.1$ becomes $\pi_\infty^{50}\tau_{1/2} =$ constant, it can be seen that the actual scaling relation for $\alpha = 0.1$ goes as $\pi_\infty^{58}\tau_{1/2} =$ constant. Thus the actual load scaling power (= 58) lies between the exponents given by Eq. (59) and Eq. (57).

A possible reason for this deviation is that while Eq. (59) applies when fiber failures occur independently of each other and Eq. (57) applies when they form by cluster extension, in reality, composite failure starts with dispersed breaking wherein Eq. (59) applies and terminates with the growth of a cluster of breaks when Eq. (57) applies. Therefore it seems reasonable that the actual scaling exponent lies between the exponents given by these extremes. Furthermore, Eq. (64) allows us to approximate the actual load scaling exponent since the dependence of the characteristic lifetime distribution on load goes as

$$W_k(\tau) \sim \pi_\infty^{\frac{\rho\beta}{\beta+((k-1)/k)\alpha/2}}\tau \tag{84}$$

so it would be reasonable to expect

$$\pi_{\infty}^{\rho\beta/(\beta+((k-1)/k)\alpha/2}\tau_{1/2} = \text{constant} \tag{85}$$

so long as the composite fails by cluster formation and growth. Setting $k = 3$ which is the observed critical cluster size in this expression for the median range, we find that the load-lifetime scaling exponent is 56.25 which is very close to the observed scaling exponent, 58.

Figure 20 shows the comparison of fiber failure times in a single specimen, using the same Monte Carlo random numbers, under three different applied loads. Fiber failure times in the composite are scaled according to Eq. (85), and while not completely converging for the three applied load levels, the last failure times are closer than when they are scaled according to Eq. (57) or Eq. (59). Note that k for each specimen is chosen to be its critical cluster size k^*. The sequence of breaks leading up to composite failure is different for the different specimens owing to the different applied loads, although they have identical standard representative random numbers. The scaling Eq. (85) is derived by statistical arguments, not deterministic ones, unlike Eq. (59) and Eq. (57). This makes the lack of collapse of the three curves unsurprising. Furthermore the limiting times are not ordered according to load level. Another contributor to the disagreement between the three scaled final lifetimes is that length scale correction, as suggested by Eq. (57), has not been incorporated into Eq. (85).

When $\alpha = 0.5$, as is evident from Figure 19, the power-law load lifetime scaling breaks down especially for smaller loads. This is to be expected, for as α increases, so does the overload length ahead of a crack prompting the dispersion of breaks in the fiber direction as often observed above. This causes the breakdown of the cluster-driven mode of composite failure, which in turn results in breakdown of the power-law load-lifetime scaling relationship.

Figure 21 shows the same scaling but of the median specimen under the three loads. Since the scaling relation is statistical, it is reasonable to compare the statistically similar median specimen although they are not the same realization in that they have different sets of standard representative random numbers for the fibers. As is seen, the failure times are close to each other; however this collapse is only approximate suggesting some non-linearity of the $\alpha = 0.1$ line in Figure 19. However, the observed mismatch of the failure times in Figure 21 is much smaller than the final mismatch in Figure 20.

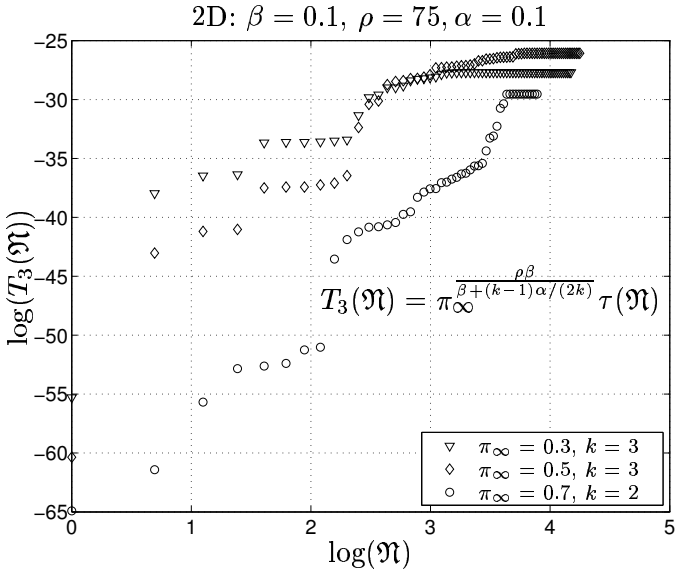

Figure 20. Damage evolution in terms of fiber failures in time in a single $\beta = 0.1$, $\rho = 75$ specimen (same standard representative random numbers) under three different loads: $\pi_\infty = 0.3$, 0.5, and 0.7. The time $\tau(\mathfrak{N})$ of occurrence of break $\mathfrak{N}$ for each applied load π_∞ is scaled according to $T_3(\mathfrak{N}) = \pi_\infty^{\rho\beta/(\beta+(k-1)\alpha/(2k))}\tau(\mathfrak{N})$ as would be expected in a load sharing bundle according to Eq. (85).

6.2. 3D Arrays

In 3D, the interaction effects of periodic images of break clusters along the fiber direction are considerably smaller than that in 2D. Hence, we assume the form for the stress concentration ahead of a k-cluster to be

$$K_k = \sqrt{\frac{\sqrt{k}}{\pi^{3/2}}\psi_k + 1} \tag{86}$$

where we have absorbed the smaller correction for periodicity (see discussion below Eq. (76))

$$1 + \exp(-\mathfrak{L}\pi\psi_1/\sqrt{k}),$$

into the factor ψ_k itself, and where Eq. (86) is derived from the form Eq. (32) for the stress concentration ahead of a staggered cluster of breaks. Also, it suffices to take ψ_k of the form

$$\psi_k = \begin{cases} 1, & \text{if } k = 1 \\ \psi & \text{if } k > 1 \end{cases} \tag{87}$$

as in 2D where ψ is left as a free fitting parameter albeit subject to the bounds $1 \leq \psi \leq 2$. In Eq. (63) we noted that the number of neighbors

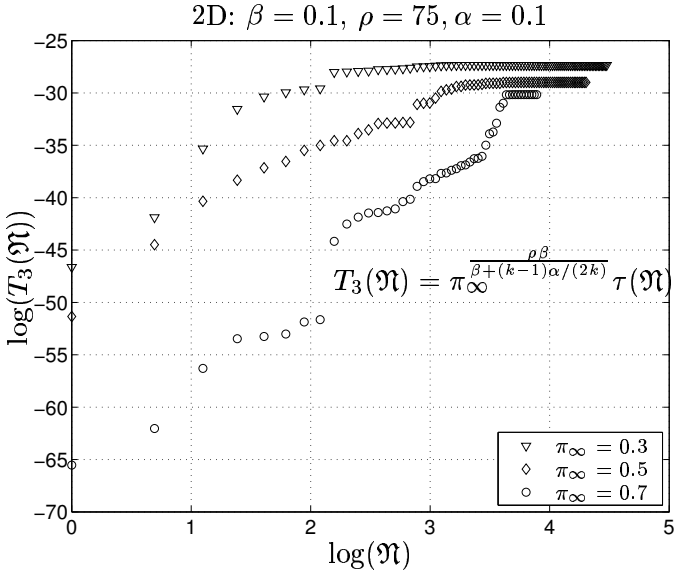

Figure 21. Damage evolution in terms of fiber failures in time in three $\beta = 0.1$, $\rho = 75$ statistically identical (median specimen among 1024 simulations; they have different standard representative random variables) specimen under three different loads: $\pi_\infty = 0.3$, 0.5, and 0.7. The scaling of fiber failure times is the same as that in Fig 20.

surrounding a j-cluster of fiber breaks is $N_j \approx (4\pi)^{1/2} j^{1/2}$. However the stress concentration varies considerably from fiber to fiber among these neighbors and in a previous work (Mahesh et al (2002)) we have found it essential to accommodate this variation by letting

$$N_j = \eta j^\nu \tag{88}$$

where η and ν are fitting parameters. N_j may be viewed as the effective number of fibers surrounding a cluster that are at high risk of failure.

Figure 22 shows a comparison of the cluster growth model against the empirical weakest link distribution obtained from simulations of an elastic matrix ($\alpha = 0$), 3D composite under applied load $\pi_\infty = 0.7$ and where $\beta = 0.1$, $\rho = 75$ for the fibers. To fit the data we have taken $N_j = 1.25 j^{0.27}$ and $\psi = 1.86$. The closeness of the fitting parameter ψ to 2 suggests that out of plane staggering of fiber breaks is minimal for this elastic matrix case with high fiber breakdown sensitivity to local fiber load level. Owing to the smaller stress concentrations ahead of a k-cluster in 3D than in 2D, the probability range of the simulations encompasses broader k^* regimes. Figure 23 similarly compares the cluster growth model with the empirical weakest-link distribution in a 3D composite with a mildly viscoelastic matrix ($\alpha = 0.1$) and fibers with

Figure 22. Comparison, on Weibull probability coordinates, of the empirical weakest-link distribution with the k-envelope given by Eq. (64) in an elastic matrix 3D composite ($\alpha = 0$) under applied load $\pi_\infty = 0.7$ and where $\beta = 0.1$, $\rho = 75$ for the fibers. To get good agreement, we set $\psi = 1.86$, $\eta = 1.25$, and $\nu = 0.27$.

a low breakdown sensitivity to local load level ($\beta = 0.5$ and $\rho = 15$) where the applied composite load is $\pi_\infty = 0.3$ per fiber. As seen, the fit is exceptionally good in the lower tail using the fitting parameter values shown in the figure. Even though the times are large, the approximate normalized overload length $\check{\omega}_k \approx \sqrt[4]{k}\tau^{\alpha/2}/2$ here is still much smaller than the normalized composite length $\mathfrak{L}$.

Generally speaking, stalling of clusters due to interactions between breaks and their periodic images is much less of an issue in 3D than in 2D arrays since these interactions are much smaller. As seen in Figure 6, stress concentration ahead of a cluster of breaks is very mildly affected as $\mathfrak{L}$ is decreased from ∞ to 5. Though not shown, the $\mathfrak{L} = 10$ line is almost indistinguishable from the $\mathfrak{L} = \infty$ line.

Figure 24 shows the lower envelope of the k-lines for 3D composites with $\beta = 0.1$ and $\rho = 75$ fibers, matrices of different creep exponents, α, and with applied load level $\pi_\infty = 0.7$. The observation and explanation in 2D regarding the order of the median lifetimes applies also in 3D.

As in 2D, the weak-linked lifetime distribution is strongly log-normal as shown in Figure 25 for $\pi_\infty = 0.3$. (Unfortunately simulation of the case of highly creep sensitive matrix, $\alpha = 0.5$, and lower load, $\pi_\infty = 0.3$, is beyond our computational capabilities so is not shown.) Unlike in 2D,

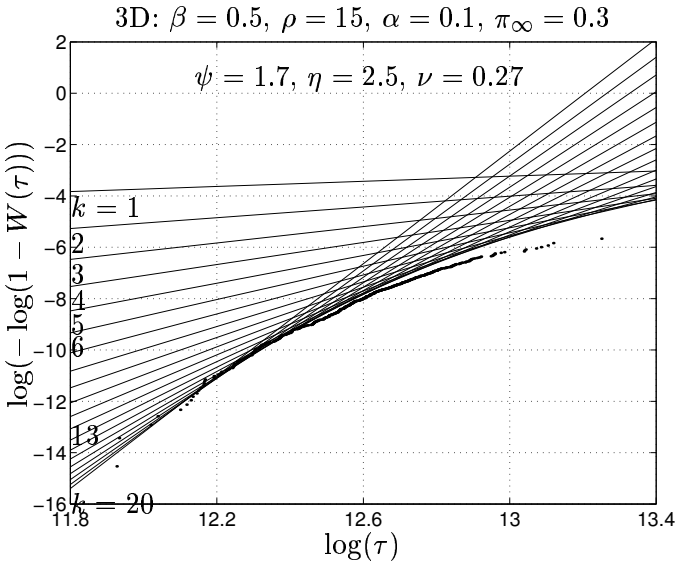

Figure 23. Comparison, on Weibull probability coordinates, of the empirical weakest-link distribution with the k-envelope given by Eq. (64) in a mildly viscoelastic matrix ($\alpha = 0.1$) 3D composite under applied load $\pi_\infty = 0.3$ and where $\beta = 0.5$, $\rho = 15$ for the fibers. To get good agreement, we set $\psi = 1.7$, $\eta = 1.25$, and $\nu = 0.27$.

log-normality of the weak-linked lifetime distribution in 3D is not tied to cluster stalling resulting from interactions between breaks and their images. This indicates that the tendency toward log-normality of the weak-linked lifetime distribution is not an artifact of our limited unit cell size for the simulations. However, what is surprising here is that $\hat{H}_{mn}$ is itself normally distributed, as shown in Figure 26, although its mean and standard deviation are far removed from the mean of 6.19×10^3 and standard deviation of 2.76×10^3 predicted by the equal load-sharing model for both $\alpha = 0$ and $\alpha = 0.1$ (since matrix characteristics are irrelevant to equal load sharing). We believe, however, that normality of $\hat{H}_{mn}(\tau)$ is coincidental and that it breaks down in the lower tail, and so, will not survive scaling to larger composites. Indications of such a breakdown are already seen among the last few specimens in Figure 26.

6.3. Discussion

For a heterogeneous material network model, very similar in breakdown and load-sharing features, Curtin and Scher (1997) showed that the failure mode of a "typical" bundle transitions from avalanche to percolation breakdown at $\rho = 2$. This result could be tied to the square-root

Figure 24. Comparison on Weibull coordinates of the empirical weakest link distribution with the minimum of the k-envelope in 3D composites with three matrix viscoelastic creep exponents $\alpha = 0$, 0.1, and 0.5 and fibers with high breakdown sensitivity to stress level $\beta = 0.1$, $\rho = 75$ and loaded under applied stress level $\pi_\infty = 0.7$. To get good agreement we have taken $\psi = 1.86$, $\eta = 1.25$, and $\nu = 0.27$.

feature of stress at the cluster tip to cluster diameter. Assuming a more severe local load sharing rule where the fiber stress at the cluster edge grew linearly with cluster size, Newman and Phoenix (2001) showed the transition to occur in their case at $\rho = 1$, and where $\beta = 1$. In the context of these studies, the composites used in the present simulations, with $\rho \geq 15$, would fall well within the avalanche regime. What the present simulations newly reveal, however, is that even within the avalanche regime, there are two types of local breakdown that trigger the avalanche, or eventual catastrophic crack growth, which we have called the clustered and dispersed modes. Thus, while the composite lifetime still has a weakest link character, Eq. (80), for both, the two modes assert themselves in the form of $\hat{W}(\tau)$ – given by the Weibull envelope in the clustered case and log-normal in the dispersed case, and in whether $\hat{m}$ is approximately mn, or is smaller. As the model parameters are changed, the transition from the clustered to the dispersed failure mode is not abrupt.

An interesting feature of the dispersed failure is mode is the existence of a log-normal, weakest-link distribution. This is likely the result of slow convergence to the normal distribution of an equal-load sharing, time-dependent bundle, which would tend toward normality if it were

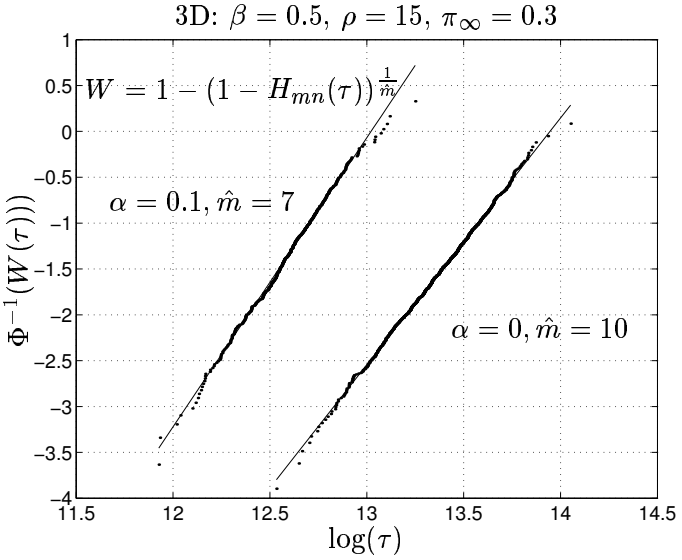

Figure 25. Plots, on log-normal coordinates, of the weak-linked empirical distribution $W(\tau)$ for composites with fibers having relatively low breakdown sensitivity to local fiber load level ($\beta = 0.5,\ \rho = 15$), matrices which are elastic ($\alpha = 0$) and mildly viscoelastic ($\alpha = 0.1$) and under relatively low applied stress $\pi_\infty = 0.3$. The linearity of the plots suggests that the weak linked distributions are log-normal.

possible to simulate sufficiently large specimens under model parameter values and load levels that proportionally increase the break cluster size needed to finally obtain catastrophic crack growth and failure. Ibnabdeljalil and Phoenix (1995) observed the persistence of log-normality in a brittle matrix composite model for much larger bundles than we have simulated, so the convergence to normality, is slow. It may very well be that in the probability range of practical interest, the weakest-link is indeed log-normal. Current computational capabilities do not permit resolving this issue in the foreseeable future.

The simulations do suggest global percolation like failure (Figure 14) when ρ and π_∞ are sufficiently small. In light of the above mentioned works, the establishment of an *accumulation time* in Eq. (79) in our finite simulation cells must be dismissed as spurious finite patch size effects. A Monte-Carlo study, similar to the present, but implementing open boundary conditions would avoid these effects. (But it would suffer from the pitfall of stress leakage out of the simulation patch, and the artificial protracted lifetimes which goes with it.) In the next section, we will calculate the form of the weakest link distribution in large composites in light of these conclusions.

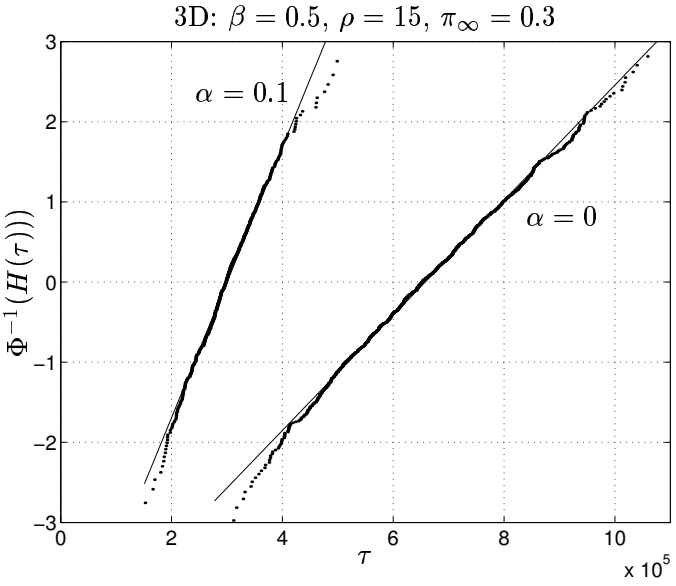

Figure 26. Plots, on normal coordinates, of the empirical distribution $H_{mn}(\tau)$ for the case of Figure 25. Except for the tails, linearity of the plot suggests normality of the distribution for these small specimens (unit cells). However, this is believed coincidental as the parameters of the normal distribution are far from those predicted by equal load-sharing theory, and the deviations in the tails will cause distortions in scaling to much larger composites.

7. Large Composites

Computational limitations have confined us to composites with $n = 100$ fibers and length $L = 10\delta_{\rm v}$, or, $mn = 1000$ fiber segments. These are very small compared to real composites, which typically have more than $mn = 10^7$ fiber segments of length of the order of $\delta_{\rm v}$. We also imposed periodic boundary conditions, which prevented stress leakage from the unit cell as would occur had we imposed patch boundary conditions, which would in turn result in artificially longer composite lifetimes. However, periodic boundary conditions resulted in spurious accumulation times owing to the interaction of breaks with their images located in close proximity. This tended to stall the growth of the sharp stress concentrations next to clusters. Furthermore, under the chain of bundles framework, we re-centered the breaks appearing in each λ-bundle both in the simulations and effectively in the modeling of cluster growth, a necessary simplification to limit computation time. To reduce the artificial effect of re-centering we set $\lambda = 0.5$ which is the smallest value given our computational constraints. While this

turned out adequate for composites with large ρ fibers (high failure sensitivity to load level), its effects were clearly discernible when ρ was smaller as it resulted in shortened overload lengths. We will consider large composites without these artificial restrictions.

7.1. 2D Arrays

When $\mathfrak{L} = \infty$, Eq. (22) and Eq. (23) express the stress concentration and overload length ahead of a k-cluster. Out of plane staggering of fiber breaks during cluster growth will still need to be accounted for and we do so by introducing the parameter ψ (compare with Eq. (76))

$$K_j(0) = \sqrt{\frac{\pi j}{8}\psi + 1}, \quad 1 \leq \psi \leq 2. \tag{89}$$

The upper bound for ψ corresponds to the case of transversely aligned breaks and the lower bound to a crack with two equally long limbs spaced substantially apart. Substituting Eq. (89) into Eq. (64), we derive the following closed form expression for $W(\tau)$ in Appendix C:

$$W(\tau) = \frac{\theta_1 \theta_3^{\theta_2}}{\tau^{\theta_5}} \exp\left\{ -\left(\frac{\rho}{2} - 1\right) \beta \frac{\theta_3}{\tau^{\theta_4}} (1 - \Theta(\tau)) \right\}, \tag{90}$$

where θ's represent constants specified in Appendix C and,

$$\Theta(\tau) = \frac{\sqrt{1/a} - 1}{(\rho/2 - 1)\beta} \frac{\tau^{\theta_4/2}}{\sqrt{\theta_3}}.$$

The composite lifetime distribution can now be obtained as usual using

$$H_{mn}(\tau) = 1 - (1 - W(\tau))^{mn} \tag{91}$$

$W(\tau)$ will not be a distribution function unless it is non-decreasing in τ. Setting $dW(\tau)/d\tau > 0$, we have a condition for its regime of validity,

$$(\rho/2 - 1)\beta\theta_3\theta_4/\tau^{\theta_4} > \theta_5. \tag{92}$$

This condition is obviously not satisfied if $\rho \leq 2$ assuming all the θ constants are positive. Interestingly our transition, 2, for ρ coincides with that of Curtin and Scher (1997) derived in an different manner.

It must be emphasized that just as Eq. (64), Eq. (90) is applicable only for large ρ. The comparisons with Monte-Carlo simulated distributions in Section 6 demonstrate its applicability down to $\rho = 15$, when finite simulation cell size effects do not affect cluster growth. In deriving the regime of validity of the clustering mode of failure and Eq. (90), we have *assumed* that although the coefficients θ_i may vary for small

ρ, the form of the expression, particularly the coefficient $\rho/2 - 1$ of the exponential term will remain unchanged. The given lower bound for applicability, $\rho = 2$ hinges on it. In the present composite model, computational constraints prevent us from verifying this assumption. We note however that it has been borne out in other studies which have assumed simpler load sharing, and fiber lifetime statistics, such as that of Newman and Phoenix (2001).

In Figure 27 we compare Eq. (90) against empirical weak-linked lifetime distributions obtained from Monte-Carlo simulations. A good fit in the case of the $\alpha = 0.5$ composite requires a ψ value slightly in excess of 2, the supposed upper bound on ψ. This is likely due to slight errors introduced during the approximations. The effect of small changes in stress concentration on lifetime is large, since lifetime scales as $K^{\rho\beta}$. Although the lower tail of the $\alpha = 0$, $W(\tau)$ distribution is a poor fit of the empirical distribution, we find that the fit improves as α is increased (and corresponding overload length decreases). This trend suggests that the failure of the $\alpha = 0$, and $\alpha = 0.1$ lower tails stems largely from the inability of Eq. (89) to capture the periodicity of boundary conditions when the overload length is sizable. In Figure 16, where more elaborate corrections for periodicity were made using Eq. (76) for the stress concentrations, the fit is much better.

An alternative form for the stress concentration, which is likely to be more successful in accounting for periodic boundary conditions while still amenable to closed form $W(\tau)$ determination, is

$$K_j(0) = \sqrt{\frac{\pi j^\nu}{8}\psi + 1}. \tag{93}$$

assigning as it does an effective crack length of ψj^ν to the j-crack, where both ψ and ν are fitting parameters to be determined in a way that results in $W(\tau)$ being a good fit to the empirical distributions.

Based on our simulation experiences, we expect that with β and α fixed, composites with large ρ will have $\psi \approx 2$. When ρ is decreased, the cluster growth will be less stress driven, prompting ψ to decrease. Similarly, ψ will decrease with increasing $\omega \propto \tau^{\alpha/2}$ for fixed ρ and β, and for fixed ρ and α will decrease with increasing β.

We imagine a cutoff ψ_c such that when $\psi < \psi_c$, failure switches from a clustered to a dispersed mode owing to insufficient hazard ahead of a cluster. The simulations suggest that the weakest link in this case is driven by the lower tail of a log-normal distribution of mean μ_1 and standard deviation σ_1, which is given by

$$\tilde{\Phi}(z(\tau)) \approx \frac{\exp\left(-z^2(\tau)/2\right)}{\sqrt{2\pi}|z(\tau)|} \tag{94}$$

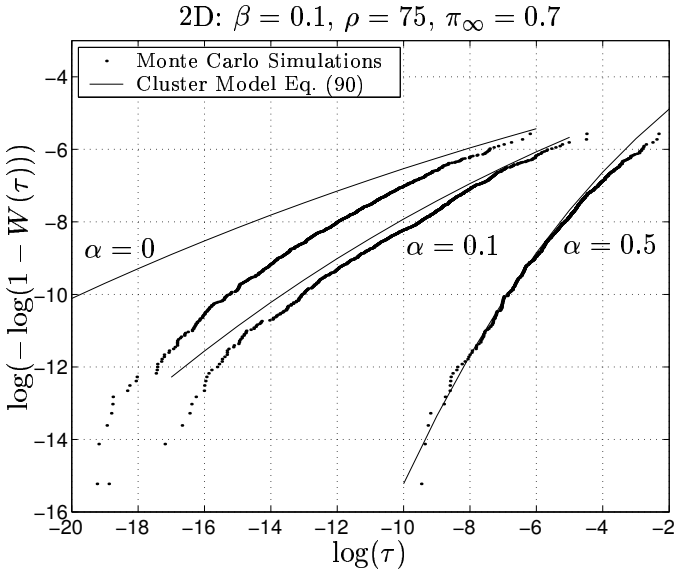

Figure 27. Comparison on Weibull paper of the empirical weakest link distribution with the 2D weakest link distribution given by Eq. (90) in $\beta = 0.1$, $\rho = 75$ fiber composites with matrix creep exponent of three different values, $\alpha = 0$, 0.1, and 0.5, under stress $\pi_\infty = 0.7$. The values of ψ used in Eq. (89) in the three cases are 1.8, 1.84, and 2.1 respectively.

where

$$z(\tau) = \frac{1}{\sigma_1} \log\left(\frac{\tau}{\exp(\mu_1)}\right).$$

The composite lifetime distribution $H(\tau)$ is given by

$$H_{\hat{m}}(z(\tau)) = 1 - \left[1 - \tilde{\Phi}(z(\tau))\right]^{\hat{m}}. \tag{95}$$

As the composite size gets large, so will $\hat{m}$. For large $\hat{m}$, from Leadbetter et al. (1983, Theorem 1.5.3) and algebraic manipulations we find

$$H(z(\tau)) = 1 - \exp\left(-\exp\{-a_{\hat{m}}(e^{-b_{\hat{m}}+z(\tau)} - 1)\}\right) \tag{96}$$

with

$$a_{\hat{m}} = (2\log\hat{m})^{1/2}$$

and

$$b_{\hat{m}} = (2\log\hat{m})^{1/2} - \frac{1}{2}(2\log\hat{m})^{-1/2}(\log\log\hat{m} + \log 4\pi).$$

This result performs poorly in practice since $\hat{m}$ must be very large.

7.2. 3D Arrays

Proceeding as in 2D, we obtain the closed form expression for $W(\tau)$ in 3D arrays in Appendix D:

$$W(\tau) \approx \frac{\theta_1 \tau^{\theta_5}}{\theta_3^{\theta_2}} \exp\left\{ -\left(\frac{\rho\beta}{4} - \beta + \nu\right) \frac{\theta_3^2}{\tau^{2\theta_4}} (1 - \Theta(\tau)) \right\} \tag{97}$$

where again, the θ's denote constants specified there, and,

$$\begin{aligned} \Theta(\tau) \approx & \frac{4a\theta_3^{-1/2}}{\rho\beta - \beta + \nu} \tau^{\theta_4/2} - \frac{4(\rho\beta - 2(\beta - \gamma) - \frac{5}{6})}{a\theta_3(\rho\beta - 4(\beta - \nu))} \tau^{\theta_4} \\ & + \frac{2(1 - 4/(3a^{3/2}))}{\theta_3^{3/2}(\rho\beta - 4(\beta - \nu))} \tau^{3\theta_4/2}. \end{aligned} \tag{98}$$

While the power of the pre-factor of the exponential, θ_5 is negative in 2D arrays, it turns positive for 3D arrays. As in 2D, in order that Eq. (97) describe a valid distribution function, it is necessary that $\rho \geq 4(1 - \nu/\beta)$. If, as in (Mahesh et al., 2002, Figure 13), $\nu \downarrow 0$ as ρ decreases, a transition from the avalanche to the percolation-type failure mode occurs near $\rho = 4$. The comments below Eq. (92) on the assumptions underlying this regime of validity result apply here too. Within the avalanche failure mode, when dispersed failure and hence log-normality of the weak-link is active, the composite distribution function is expected to be independent of composite dimensionality, and therefore to obey Eq. (96).

The approximations involved in obtaining Eq. (97), especially in Eq. (174) and Eq. (175) are more severe than those involved in obtaining Eq. (90). The present approximations improve for larger k than can be simulated with current computational capabilities. Comparison of Eq. (97) with the simulated 3D lifetime distributions is thus necessarily poor, and is not shown. We give the result, however, in anticipation that the sizes of composites that can be simulated will eventually be large enough for a fair comparison. We note that the envelope forms from which Eq. (97) was derived do indeed work well.

8. Conclusion

Using Monte-Carlo simulations as a guide, we have developed analytical models for the lifetime distributions of 2D and 3D fiber composites with Coleman fibers and a viscoelastic matrix. This was done within the avalanche regime of Curtin and Scher (1997). Unlike many earlier

models, we have not confined fiber failures to a single plane transverse to the fiber direction. The conclusions arrived at through Monte-Carlo simulations are summarized in Section 6.3. The values of ρ at which the analytical lifetime distribution functions, Eqs. (90), and (97), calculated assuming clustered failure mode breakdown and when regarded as the point of transition from the "avalanche" to the "percolation" failure mode of Curtin and Scher (1997), result in the critical values $\rho = 2$ in 2D, and $\rho \approx 4$ in 3D composites, respectively. The validity of this interpretation however remains to be seen, and given the implausibility of simulating this limit in the foreseeable future, only detailed analytical calculations may be able to prove it.

Acknowledgements

SLP acknowledges support from the Institute for Future Space Transport funded under a NASA URETI grant and monitored through NASA Glenn Research Center. SM acknowledges support from the DOE, Office of Science, Office of Basic Energy Sciences. This research was conducted using the resources of the Cornell Theory Center, which receives funding from Cornell University, New York State, federal agencies, foundations, and corporate partners.

References

Beyerlein, I. J. and S. L. Phoenix: 1997a, 'Statistics of fracture for an elastic notched composite lamina containing Weibull fibers — I'. *Engineering Fracture Mechanics* pp. 241–265.

Beyerlein, I. J. and S. L. Phoenix: 1997b, 'Statistics of fracture for an elastic notched composite lamina containing Weibull fibers — II'. *Engineering Fracture Mechanics* **57**, 267–299.

Beyerlein, I. J., S. L. Phoenix and R. Raj: 1998, 'Time evolution of stress redistribution around multiple fiber breaks in a composite with viscous and viscoelastic matrices'. *International Journal of Solids and Structures* **35**, 3177–3211.

Coleman, B. D.: 1956, 'Time dependence of mechanical breakdown phenomena'. *Journal of Applied Physics* **27**, 862–866.

Coleman, B. D.: 1957a, 'A stochastic process model for material breakdown'. *Transactions of the Society of Rheology* **1**, 153–168.

Coleman, B. D.: 1957b, 'Time dependence of mechanical breakdown of fibers I. Constant total load'. *Journal of Applied Physics* **28**, 1058–1064.

Coleman, B. D.: 1958a, 'On the strength of classical fibers and fiber bundles'. *Journal of the Mechanics and Physics of Solids* **7**, 60–70.

Coleman, B. D.: 1958b, 'Statistical and time-dependent mechanical breakdown of fibers'. *Journal of Applied Physics* **7**, 60–70.

Copson, E. T.: 1965, *Asymptotic Expansions.* Cambridge: University Press.

Curtin, W. A.: 1998, 'Size scaling of strength in heterogeneous materials'. *Physical Review Letters* **80**(7), 1445–1448.

Curtin, W. A., M. Pamel, and H. Scher: 1997, ' Time-dependent damage evolution and failure in materials. II. Simulations '. *Physical Review B* **55**, 12051–12061.

Curtin, W. A. and H. Scher: 1991, 'Analytic model for scaling of breakdown'. *Physical Review Letters* **67**, 2457–2460.

Curtin, W. A. and H. Scher: 1997, 'Time-dependent damage evolution and failure in materials. I. Theory'. *Physical Review B* **55**, 12038–12050.

Goda, K.: 2001, 'Application of Markov process to chain-of-bundles probability model and lifetime distribution analysis for fibrous composites'. *Materials Science Research International* **STP-2**, 242–249.

Goda, K.: 2003, 'A strength reliability model by Markov process of unidirectional composites with fibers placed in hexagonal arrays'. *International Journal of Solids and Structures* **40**, 6813–6833.

Hedgepeth, J. M.: 1961, 'Stress concentrations in filamentary structures'. Technical Report TND-882, NASA.

Hedgepeth, J. M. and P. V. Dyke: 1967, 'Local stress concentrations in imperfect filament composites'. *Journal of Composite Materials* **1**, 294–309.

Horn, R. A. and C. R. Johnson: 1985, *Matrix Analysis*. Cambridge University Press, Cambridge.

Ibnabdeljalil, M. and S. L. Phoenix: 1995, 'Creep rupture of brittle matrix composites reinforced with time dependent fibers: scalings and Monte Carlo simulations'. *Journal of the Mechanics and Physics of Solids* **43**, 897–931.

Lagoudas, D. C., S. L. Phoenix, and C.-Y. Hui: 1989, 'Time evolution of overstress profiles near broken fibers in a composite with a viscoelastic matrix'. *International Journal of Solids and Structures* **25**, 45–66.

Landis, C. M., I. J. Beyerlein, and R. M. McMeeking: 2000, 'Micromechanical simulation of the failure of fiber reinforced composites'. *Journal of the Mechanics and Physics of Solids* **48**, 621–648.

Leadbetter, M. R., G. Lindgren, and H. Rootzén: 1983, *Extremes and related properties of random sequences and processes*. New York: Springer.

Mahesh, S., I. J. Beyerlein, and S. L. Phoenix: 1999, 'Size and heterogeneity effects on the strength of fibrous composites'. *Physica D* **133**, 371–389.

Mahesh, S., S. L. Phoenix, and I. J. Beyerlein: 2002, 'Strength distributions and size effects for 2D and 3D composites with Weibull fibers in an elastic matrix'. *International Journal of Fracture* **115**, 41–85.

Newman, W. I. and S. L. Phoenix: 2001, 'Time-dependent fiber bundles with local load sharing'. *Physical Review E* **63**, 021507.

Phoenix, S. L.: 1978, 'The asymptotic time to failure of a mechanical system of parallel members.'. *SIAM Journal of Applied Mathematics* **34**, 227–246.

Phoenix, S. L. and L. Tierney: 1983, 'A statistical model for the time dependent failure of unidirectional composite materials under local elastic load-sharing among fibers'. *Engineering Fracture Mechanics* **18**, 193–215.

Smith, R. L.: 1980, 'A probability model for fibrous composites with local load sharing'. *Proceedings of the Royal Society of London* **373**, 539–553.

Tierney, L.: 1980, 'Limit theorems for the failure time of bundles of fibers under unequal load sharing'. Ph.D. thesis, Cornell University, Ithaca, New York.

Tierney, L.: 1982, 'Asymptotic bounds on the time to fatigue failure of bundles of fibers under local load sharing'. *Advances in Applied Probability* **56**, 95–121.

Wu, B. Q. and P. L. Leath: 2000, 'Similarity of growing cracks in breakdown of heterogeneous planar interfaces'. *Physical Review B* **62**, 9338.

Appendix

A. Solution of the Governing Equations

Here we detail the solution of the governing equation Eq. (13) subject to the boundary conditions Eqs. (15-18). In Section A.2, we solve the problem of determining stresses in a periodic patch in the presence of a single fiber break and in Section A.3, we detail the approach to superpose single break solutions in order to handle multiple interacting breaks which may or may not all form at once. First, however, in Section A.1 we express the boundary value problem in non-dimensional terms by a suitable change of variables.

A.1. Normalized Equations and Boundary Conditions

We define the important quantities φ and $\delta_{\rm v}$, respectively, as

$$\varphi = \max_{\substack{1\le i,j\le n \\ i\neq j}} \varphi_{ij}, \tag{99}$$

and

$$\delta_{\rm v} = \sqrt{\frac{E_{\rm f} A_{\rm f} J_{\rm e}}{\varphi}}, \tag{100}$$

where $\delta_{\rm v}$ is a viscoelastic characteristic length scale and is approximately the length of the unloading zone around a fiber break at time $t_{\rm cm}$ after its formation. Correspondence is made between the elastic and viscoelastic matrix problems by choosing the parameters of the creep compliance such that $\delta_{\rm v} \approx \delta_{\rm e} \approx \sqrt{EA/G\varphi}$ where G is the elastic shear modulus. In terms of these quantities we define normalized variables ϕ_{ij}, ξ, σ_i and U_i, for $1 \le i, j \le n$ as

$$\phi_{ij} = \frac{\varphi_{ij}}{\varphi} \tag{101}$$

$$\xi = \frac{x}{\delta_{\rm v}} \tag{102}$$

$$\tau = \frac{t}{t_{cm}} \tag{103}$$

$$\mathscr{G}_{\rm m}(\tau) = \frac{G(\tau t_{\rm cm})}{G_{\rm e}} \tag{104}$$

$$\sigma_i(\xi,\tau) = \frac{p_i(\xi\delta_{\rm v}, \tau t_{\rm cm})}{p_\infty} \tag{105}$$

$$U_i(\xi,\tau) = u_i(\xi\delta_{\rm v}, \tau t_{\rm cm})\frac{E_{\rm f}A_{\rm f}}{p_\infty \delta_{\rm v}} \tag{106}$$

The normalization of u_i is such that Hooke's law takes on the form

$$\frac{\partial U_i}{\partial \xi} = \sigma_i. \tag{107}$$

From Eq. (102), the normalized composite unit cell length becomes

$$\mathfrak{L} = \frac{L}{\delta_{\rm v}}. \tag{108}$$

Also from Eq. (9), Eq. (12), and Eq. (101) it follows that for 2D arrays,

$$\phi_{ij} = \begin{cases} -2 & \text{if } i = j, \\ 1 & \text{if } |i-j| \mod n = 1, \\ 0 & \text{otherwise} \end{cases} \tag{109}$$

Similarly, for 3D arrays, Eq. (10), Eq. (12), and Eq. (101) yield

$$\varphi_{(\ell_1,m_1),(\ell_2,m_2)} = \begin{cases} -6 & \text{if } \ell_1 = \ell_2 \text{ and } m_1 = m_2, \\ 1 & \text{if } \max((\ell_1-\ell_2) \mod \sqrt{n}, (m_1-m_2) \mod \sqrt{n}) = 1, \\ 0 & \text{otherwise.} \end{cases} \tag{110}$$

With these normalizations, the governing equation Eq. (11) becomes

$$\frac{\partial^2 U_i(\xi,\tau)}{\partial \xi^2} + \int_0^\tau \mathscr{G}_{\rm m}(\tau - v)\left(\sum_{j=1}^{n}\phi_{ij}\frac{\partial U_j(\xi,v)}{\partial v}\right)dv = 0, \quad i = 1,2,\ldots,n \tag{111}$$

Normalizing the boundary conditions Eq. (15)–Eq. (18), yields

$$\sigma_i(\xi = 0,\tau) = \sigma_i(\xi = \mathfrak{L},\tau), \quad \tau \geq 0, \quad i = 1,\ldots,n \tag{112}$$

$$\sigma_{i_k} = \frac{\partial U_{i_k}(\xi_j)}{\partial \xi} = 0, \quad (i_k,\xi_k) \in B, \quad k = 1,\ldots,r \tag{113}$$

$$U_i(\xi = 0,\tau) = U_i(\xi = \mathfrak{L},\tau) + C(\tau) \quad (i,0) \notin B \tag{114}$$

and

$$\sum_{i=1}^{n}\sigma_i(\xi,\tau) = n, \quad 0 \leq \xi \leq \mathfrak{L}, \quad \tau \geq 0. \tag{115}$$

where $C(\tau)$ is the normalized version of $c(t)$ in Eq. (16).

To cast the problem in influence function terms, we consider an 'auxiliary' problem whereby the far field load is eliminated but a *compressive* force of magnitude p_∞ is applied to each end at a fiber break, forcing each break open. In normalized variables this becomes a unit compressive force. The effect is to uniformly reduce the strains by p_∞/E_f, stresses by p_∞ and, displacements by $p_\infty x/E_\mathrm{f}$. Thus we let $U_i'(\xi,\tau)$ be the fiber displacement in the auxiliary problem and have

$$U_i'(\xi,\tau) = U_i(\xi,\tau) - \xi \tag{116}$$

Taking $\sigma_i' = \partial U_i'/\partial\xi$ (primes do not denote differentiation) we have

$$\sigma_i'(\xi) = \sigma_i(\xi) - 1. \tag{117}$$

To obtain U_i', we must solve the system of differential equations

$$\frac{\partial^2 U_i'(\xi,\tau)}{\partial\xi^2} + \int_0^\tau \mathscr{G}_\mathrm{m}(\tau - v)\left(\sum_{j=1}^{n}\phi_{ij}\frac{\partial U_j'(\xi,v)}{\partial v}\right)dv = 0, \qquad i = 1,2,\ldots,n \tag{118}$$

subject to the boundary conditions

$$\sigma_i'(\xi = 0,\tau) = \sigma_i'(\xi = \mathfrak{L},\tau), \quad \tau \geq 0, \quad (i,0) \notin B \tag{119}$$

$$U_i'(\xi = 0,\tau) = U_i'(\xi = \mathfrak{L},\tau) + C(\tau), \quad (i,0) \notin B \tag{120}$$

$$\sigma_{i_k}' = \frac{\partial U_{i_k}'(\xi_k)}{\partial\xi} = -1, \quad (i_k,\xi_k) \in B, \quad k = 1,\ldots,r \tag{121}$$

and

$$\sum_{i=1}^{n}\sigma_i'(\xi,\tau) = 0, \quad \tau \geq 0, \quad 0 \leq \xi \leq \mathfrak{L}. \tag{122}$$

The stress field $\sigma_i'(\xi,\tau)$ is thus the stress in a periodic patch due to a unit normalized compressive load forcing open each break but with no far field load applied. The benefit is that σ_i gives the influence of the compressive forces applied at the breaks in B on fiber i at ξ. Once U_i' is known we can obtain the displacement field due to the far-field unit normalized tensile load using Eq. (116) and Eq. (117). In the next section, we give the solution for a single break and in Section A.3 we extend this to multiple breaks by linear superposition.

A.2. Single Break Solution

The solution to the multiple break problem can be built up from a special 'unit' auxiliary problem, where a single break occurs at time

$t = 0$ in fiber $i = i_0$ at position $\xi = 0$. To emphasize this restriction, we $V_i'(\xi, \tau)$ denote the displacement $U_i'(\xi, \tau)$ in fiber i at position ξ and time τ due to this single break, and let $\bar{V}_i(\xi, s)$ be the Laplace transform of $V_i'(\xi, \tau)$, $i = 1, \ldots, n$. Thus

$$\bar{V}_i(\xi, s) = \int_0^\infty V_i'(\xi, \tau) e^{-s\tau} d\tau. \tag{123}$$

In terms of $\bar{V}_i(\xi, s)$ then, Eq. (118) becomes

$$\frac{\partial^2 \bar{V}_i(\xi, s)}{\partial \xi^2} + s\bar{\mathscr{G}}_{\mathrm{m}}(s) \left(\sum_{j=1}^{n} \phi_{ij} \bar{V}_j(\xi, s) \right) = 0, \quad i = 1, \ldots, n. \tag{124}$$

The boundary conditions Eq. (119) to Eq. (122) now become

$$\frac{\partial \bar{V}_i}{\partial \xi}(0, s) = \frac{\partial \bar{V}_i}{\partial \xi}(\mathfrak{L}, s), \quad s \geq 0, \quad i = 1, 2, \ldots, n. \tag{125}$$

$$\bar{V}_i(0, s) = \bar{V}_i(\mathfrak{L}, s) + \bar{C}_0(s), \quad s \geq 0, \quad i \neq i_0 \tag{126}$$

$$\frac{\partial \bar{V}_i}{\partial \xi}(0, s) = -\frac{1}{s}, \quad s \geq 0, \quad i = i_0 \tag{127}$$

and

$$\sum_{i=1}^{n} \frac{\partial \bar{V}_i}{\partial \xi}(\xi, s) = 0, \quad 0 \leq \xi \leq \mathfrak{L}, \quad s \geq 0. \tag{128}$$

where $C_0(\tau)$ is $C(\tau)$ corresponding to the single break case. For the power law matrix creep function, we have

$$s\bar{\mathscr{G}}(s) = \frac{s^\alpha}{\Gamma(1+\alpha)}, \quad \alpha \geq 0. \tag{129}$$

In terms of the vector $\bar{\mathbf{V}} = \{\bar{V}_1, \bar{V}_2, \cdots, \bar{V}_n\}^T$, and the matrix $\mathbf{\Phi} = [\phi_{ij}]$, Eq. (124) can be rewritten as

$$\left(\frac{\sqrt{\Gamma(1+\alpha)}}{s^{\alpha/2}} \right)^2 \frac{\partial^2}{\partial \xi^2} \{\bar{\mathbf{V}}\} - [\mathbf{\Phi}]\{\bar{\mathbf{V}}\} = \{\mathbf{0}\}. \tag{130}$$

To solve Eq. (130), we need the eigenvalues and eigenvectors of $\mathbf{\Phi}$, which is a symmetric, diagonal-dominant matrix with zero row (and column) sums. Thus the eigenvalues $\lambda_i^2, i = 1, \ldots, n$ are real and by Gershgorin's theorem, $\lambda_i^2 \in [0, 2\max_{1 \leq i \leq n} |\phi_{ii}|), i = 1, 2, \ldots, n$. We also assume the system is semi-connected, i.e., given any distinct integers p, and q, there is a sequence $p = k_1$, k_2, ..., $k_m = q$, such that matrix

entries $\phi_{k_1k_2}$, $\phi_{k_2k_3}$, ..., $\phi_{k_{m-1}k_m}$ are non-zero. Since $\lambda_1 = 0$ lies on the boundary of the Gershgorin disk, to it corresponds the eigenvector $\mathbf{1} = \{11\ldots1\}^T$, unique up to a multiplicative constant. Thus, the null space of $\mathbf{\Phi}$ is 1D with basis $\mathbf{1}$. The remaining $n-1$ eigenvectors are orthogonal to $\mathbf{1}$, so their rows sum identically to zero.

Let the normalized right eigenvectors of matrix $[-\mathbf{\Phi}]$ be $\mathbf{E}_j$, $j = 1, 2, \ldots, n$ corresponding to eigenvalues λ_j^2, $j = 1, 2, \ldots, n$ where the normalization can, for example, be done so that $\sum_{i=1}^{n} |E_{ij}| = n$ for each i and $\lambda_1 = 0$, and $\mathbf{E}_1 = \mathbf{1}$. The solution to Eq. (130) is

$$\bar{\mathbf{V}}(\xi, s) = \frac{1}{s^{1+\alpha/2}} \{e_1 \mathbf{E}_1 + \sum_{j=2}^{n} e_j \mathbf{E}_j \left[\exp\left(-\frac{\lambda_j s^{\alpha/2} \xi}{\sqrt{\Gamma(1+\alpha)}} \right) - \exp\left(\frac{\lambda_j s^{\alpha/2} (\xi - \mathfrak{L})}{\sqrt{\Gamma(1+\alpha)}} \right) \right] \} \tag{131}$$

where $e_j \equiv e_j(s)$, $j = 1, 2, \ldots, n$ are scalar multiples of the eigenvectors which must be chosen appropriately. Also

$$\frac{\partial \bar{\mathbf{V}}}{\partial \xi}(\xi, s) = \frac{1}{s} \left\{ \sum_{j=2}^{n} e_j \mathbf{E}_j \frac{\lambda_i}{\sqrt{\Gamma(1+\alpha)}} \times \left[-\exp\left(-\frac{\lambda_i s^{\alpha/2} \xi}{\sqrt{\Gamma(1+\alpha)}} \right) - \exp\left(\frac{\lambda_j s^{\alpha/2} (\xi - \mathfrak{L})}{\sqrt{\Gamma(1+\alpha)}} \right) \right] \right\}. \tag{132}$$

Boundary conditions Eq. (125) and Eq. (128) are already satisfied by this solution, the former being obvious by substitution and latter since the row sum of each eigenvector other than the first is zero. To satisfy Eq. (126) and Eq. (127), we scale the eigenvectors $\mathbf{E}_i, i = 1, 2, \ldots, n$ by choosing e_i appropriately. Eq. (126) is satisfied for $i \neq i_0$ by taking

$$e_1 E_{i1} + \sum_{j=2}^{n} e_j E_{ij} \left[1 - \exp\left(-\frac{\lambda_j s^{\alpha/2} \mathfrak{L}}{\sqrt{\Gamma(1+\alpha)}} \right) \right] = 0, \quad 0 \leq s < \infty \tag{133}$$

and Eq. (128) is satisfied by taking

$$\sum_{j=2}^{n} \frac{\lambda_j}{\sqrt{\Gamma(1+\alpha)}} e_j E_{i_0 j} \left[-1 - \exp\left(-\frac{\lambda_j s^{\alpha/2} \mathfrak{L}}{\sqrt{\Gamma(1+\alpha)}} \right) \right] = -1, \quad 0 \leq s < \infty. \tag{134}$$

Eq. (133) and Eq. (134) together give n linear equations to solve for the n unknowns e_j, $j = 1, \ldots, n$ at any s.

Obtaining normalized stresses and displacements in the time domain requires inverting Eq. (131) and Eq. (132). Exact inversion is

intractable, but Schapery's direct method for approximate Laplace inversion yields

$$f(t) = s\,\bar{f}(s)\big|_{s=e^{-\gamma}/t} \tag{135}$$

where $\gamma \approx 0.577$ is Euler's constant. Beyerlein et al. (1998) discuss the regime of validity of Schapery's approximate inverse formula. In terms of this approximate inverse, the solution becomes

$$\begin{aligned}\mathbf{V}'(\xi,\tau) =& \frac{\tau^{\alpha/2}}{\mu}\{e_1\mathbf{E}_1 \\ &+ \sum_{j=2}^{n} e_j\mathbf{E}_j\left[\exp\left(-\frac{\lambda_j\mu\xi}{\tau^{\alpha/2}\sqrt{\Gamma(1+\alpha)}}\right) - \exp\left(\frac{\lambda_j\mu(\xi-\mathfrak{L})}{\tau^{\alpha/2}\sqrt{\Gamma(1+\alpha)}}\right)\right]\Bigg\}\end{aligned} \tag{136}$$

and

$$\begin{aligned}\frac{\partial\mathbf{V}'}{\partial\xi}(\xi,\tau) =& \Bigg\{\sum_{j=2}^{n} e_j\mathbf{E}_j\frac{\lambda_j}{\sqrt{\Gamma(1+\alpha)}} \\ &\times\left[-\exp\left(-\frac{\lambda_j\mu\xi}{\tau^{\alpha/2}\sqrt{\Gamma(1+\alpha)}}\right) - \exp\left(\frac{\lambda_j\mu(\xi-\mathfrak{L})}{\tau^{\alpha/2}\sqrt{\Gamma(1+\alpha)}}\right)\right]\Bigg\}\end{aligned} \tag{137}$$

where

$$\mu = e^{-\gamma\alpha/2} \tag{138}$$

and $\mathbf{E}_j$, $j = 1, 2, \ldots, n$ are scaled so that

$$e_1E_{i1} + \sum_{j=2}^{n} e_jE_{ij}\left[1 - \exp\left(-\frac{\lambda_j\mu\mathfrak{L}}{\tau^{\alpha/2}\sqrt{\Gamma(1+\alpha)}}\right)\right] = 0, \quad 0 \le \tau < \infty \tag{139}$$

and

$$\sum_{j=2}^{n}\frac{\lambda_j}{\sqrt{\Gamma(1+\alpha)}}e_jE_{i_0j}\left[-1 - \exp\left(-\frac{\lambda_j\mu\mathfrak{L}}{\tau^{\alpha/2}\sqrt{\Gamma(1+\alpha)}}\right)\right] = -1, \quad 0 \le \tau < \infty. \tag{140}$$

Note that the $e_j \equiv e_j(\tau)$ represent time varying scales for the $\mathbf{E}_j$.

Since we need the solution for an arbitrarily located break in the periodic cell, we make explicit the notation for the break at $(i_0, \xi = 0)$ as

$$V_j(\xi,\tau) = V_j(\xi,\tau;i_0,0), \tag{141}$$

where, in accordance with Eq. (116), $V_j(\xi,\tau) = V_j'(\xi,\tau) + \xi$. The displacement due to a single break at $(i_0, \xi^\sharp)$, denoted by $U_j^\sharp(\xi,\tau;i_0,\xi^\sharp)$

for $0 \le \xi^\sharp \le \mathfrak{L}$, is obtained by translating $V_j(\xi, \tau; i_0, 0)$ as

$$U_j^\sharp(\xi, \tau; i_0, \xi^\sharp) = V_j((\xi - \xi^\sharp) \bmod \mathfrak{L}, \tau; i_0, 0). \tag{142}$$

A computationally attractive feature of the 2D and 3D arrays of Section 1.1 under periodic boundary conditions is that translational invariance holds also in the transverse direction. In 2D it suffices to carry out the above analysis for a break at $\ell = 0$, $\xi = 0$ and determine $V_\ell(\xi, \tau; 0, 0)$. The displacement of fiber ℓ, denoted $U^\sharp(\ell, \xi, \tau; \ell^\sharp, \xi^\sharp)$ due to a break at $\ell = \ell^\sharp$, and $\xi = \xi^\sharp$ is given by

$$U^\sharp(\ell, \xi, \tau; \ell^\sharp, \xi^\sharp) = V_\ell((\ell - \ell^\sharp) \bmod n, (\xi - \xi^\sharp) \bmod \mathfrak{L}, \tau; 0, 0). \tag{143}$$

Similarly in 3D, the displacement $U^\sharp(\ell, m, \xi, \tau; \ell^\sharp, m^\sharp, \xi^\sharp)$ of fiber (ℓ, m) due to a break at $\ell = \ell^\sharp$, $m = m^\sharp$, and $\xi = \xi^\sharp$ is given by

$$U^\sharp(\ell, m, \xi, \tau; \ell^\sharp, m^\sharp, \xi^\sharp) = V_\ell((\ell - \ell^\sharp) \bmod \sqrt{n}, (m - m^\sharp) \bmod \sqrt{n}, (\xi - \xi^\sharp) \bmod \mathfrak{L}, \tau; 0, 0). \tag{144}$$

In general, under other types of boundary conditions, simple solution translation is inadequate and the entire procedure described above must be carried out for each fiber.

Next we consider the superposition of single break solutions to determine the stress state due to r fiber breaks formed at different times.

A.3. Multiple Break Solution

Through weighted superposition of single break solutions, we wish to determine the displacement and stress state in a periodic composite cell at normalized time $\tau \ge \tau_r$ due to r breaks formed at normalized times $\tau_1 \le \tau_2 \le \ldots \le \tau_r$ and located at (i_1, ξ_1), (i_2, ξ_2), ..., (i_r, ξ_r). For $1 \le i, j \le r$, let $\Lambda_{ij}(\tau)$ denote the normalized stress at the location of fiber break j due to a unit compressive load applied at fiber break i at normalized time τ from initial load application. That is, let

$$\Lambda_{ij}(\tau) = \frac{\partial V_j}{\partial \xi}(\xi_j, \tau; i, \xi_i) \tag{145}$$

be the influence at (j, ξ_j) due a break at (i, ξ_i) as determined by Eq. (137) in the notation of Eq. (141). We must find weighting functions $w_i(\zeta), i = 1, 2, \ldots, r$ such that

$$-1 = \sum_{\substack{i=1 \\ \tau_i \le \tau}}^{r} \left[\Lambda_{ij}(\tau - \tau_i) w_i(\tau_i) + \int_{\tau_i}^{\tau} \Lambda_{ij}(\tau - \zeta) \frac{\partial w_i(\zeta)}{\partial \zeta} d\zeta \right], \quad j = 1, 2, \ldots, r. \tag{146}$$

Analytical solution for $w_i(\zeta)$, $i \in \{1, 2, \ldots, r\}$ and $0 \leq \zeta \leq \tau$ is generally intractable. A numerical method consists of stepping though normalized time from $\zeta = 0$ to $\zeta = \tau$ as follows: For $k > r$ define $0 = \zeta_0 < \zeta_1 < \ldots < \zeta_k = \tau$, as a partition of time interval $[0, \tau]$ such that for each τ_i, $i = 1, \ldots, r$, there is a ζ_{p_i} such that $\tau_i = \zeta_{p_i}$. Then, we approximately express condition Eq. (146) in terms of the ζ_i's as

$$-1 = \sum_{\substack{i=1 \\ \tau_i \leq \tau}}^{r} \left[\Lambda_{ij}(\tau - \tau_i) w_i(\tau_i) + \sum_{m=p_i+1}^{k} \Lambda_{ij}(\tau - \zeta_m) \left(w_i(\zeta_m) - w_i(\zeta_{m-1}) \right) \right], \quad j = 1, 2, \ldots, r. \tag{147}$$

The choice of ζ_i, $i = 1, \ldots, k$ determines the accuracy and speed of the numerical approximation as discussed below. Beyerlein et al. (1998) discuss merits and drawbacks of various methods. In terms of

$$\begin{aligned} C_j(\tau) = -1 - \sum_{\substack{i=1 \\ \tau_i \leq \tau}}^{r} \Bigg[& \Lambda_{ij}(\tau - \tau_i) w_i(\tau_i) - \Lambda_{ij}(0^+) w_i(\zeta_{k-1}) \\ & + \sum_{m=p_i+1}^{k-1} \Lambda_{ij}(\tau - \zeta_m) \left(w_i(\zeta_m) - w_i(\zeta_{m-1}) \right) \Bigg], \\ & j = 1, 2, \ldots, r, \end{aligned} \tag{148}$$

Eq. (147) can be rewritten as a matrix equation

$$[\mathbf{\Lambda}(0^+)]\{\mathbf{w}(\tau)\} = \{\mathbf{C}(\tau)\} \tag{149}$$

where $\mathbf{\Lambda}(0^+)$ is the matrix of instantaneous influences of the r breaks on each other, $\mathbf{C} = \{C_1, C_2, \ldots, C_r\}^T$ and $\mathbf{w} = \{w_1, w_2, \ldots, w_r\}^T$. This system of equations can then be solved for the weights $w_j(\tau)$, $j = 1, \ldots, r$. It can be shown that $[\mathbf{\Lambda}(0^+)]$ is negative definite.

B. Asymptotic Approximation of $W_k(\tau)$ for large ρ

Here we detail the asymptotic approximation for λ^* in Eq. (61) for large ρ. In that case, by combining Eq. (60) and Eq. (61) we have

$$W_k(\tau) = 2^k \Gamma(1+\beta)^k \Gamma(1+k\beta)^{-1} \pi_\infty^{k\rho\beta} \tau^{k(\beta+\alpha/2)} \prod_{j=0}^{k-1} \left[N_j \int_0^{\frac{\lambda'}{2\tau^{\alpha/2}}} d\xi \left\{ \int_0^1 [1 + (K_j(0) - 1) \exp(-\xi c_j / \zeta^{\alpha/2})]^\rho d\zeta \right\}^\beta \right]. \tag{150}$$

When $\alpha = 0$, the double integral collapses simply into the single integral

$$P_j = \int_0^{\frac{\lambda'}{2}} d\xi [1 + (K_j(0) - 1)\exp(-\xi c_j)]^{\rho\beta}. \tag{151}$$

For $\alpha > 0$, the integral in the product above may be approximated as

$$\begin{aligned} P_j &= \int_0^{\frac{\lambda'}{2\tau^{\alpha/2}}} d\xi \left\{ \int_0^1 [1 + (K_j(0) - 1)\exp(-\xi c_j/\zeta^{\alpha/2})]^\rho d\zeta \right\}^\beta \\ &= (\theta - 1)^\beta \int_0^{\frac{\lambda'}{2\tau^{\alpha/2}}} d\xi \left\{ \int_0^\infty \frac{[1 + (K_j(0) - 1)\exp(-\xi c_j(w+1))]^\rho}{w^\theta} dw \right\}^\beta \\ &= \frac{(\theta - 1)^\beta}{c_j} \int_0^{\frac{\lambda' c_j}{2\tau^{\alpha/2}}} d\mu_j \left\{ \int_0^\infty \frac{[1 + \mathfrak{C}_j \exp(-\mu_j w)]^\rho}{(w+1)^\theta} dw \right\}^\beta \end{aligned} \tag{152}$$

upon making the change of variable $w = \zeta^{-\alpha/2} - 1$ where $\theta = 2/\alpha + 1$ in the first step and $\xi c_j = \mu_j$ in the second, and abbreviating $(K_j(0) - 1)\exp(-\mu_j) = \mathfrak{C}_j$. When ρ is large we can accurately approximate the inner integral as

$$\begin{aligned} \int_0^\infty \frac{[1 + \mathfrak{C}_j \exp(-\mu_j w)]^\rho}{(w+1)^\theta} dw &= (1 + \mathfrak{C}_j)^\rho \int_0^\infty \frac{\left[1 - \frac{\mathfrak{C}_j}{\mathfrak{C}_j + 1}(1 - e^{-\mu_j w})\right]^\rho}{(w+1)^\theta} dw \\ &\approx (1 + \mathfrak{C}_j)^\rho \int_0^\infty \frac{\exp(-\mathfrak{C}_j \mu_j \rho w/(\mathfrak{C}_j + 1))}{(w+1)^\theta} dw \\ &\approx (1 + \mathfrak{C}_j)^\rho \int_0^\infty \exp\left(-\frac{\mathfrak{C}_j \mu_j \rho w}{\mathfrak{C}_j + 1} - \theta \log(w+1) \right) dw \\ &\approx (1 + \mathfrak{C}_j)^\rho \int_0^\infty \exp\left(-\frac{\mathfrak{C}_j \mu_j \rho w}{\mathfrak{C}_j + 1} - \theta w \right) dw \\ &= \frac{(1 + \mathfrak{C}_j)^{\rho+1}}{\theta + \mathfrak{C}_j(\theta + \rho\mu_j)}. \end{aligned} \tag{153}$$

Whereas $[1 + \mathfrak{C}_j \exp(-\mu_j w)]^\rho > 1$ for all $w \geq 0$, our exponential approximation in the second step including $(1 + \mathfrak{C}_j)^{\rho+1}$ tends to zero for large w. To account for this disparity, we notice that the exponential factor dips below one at $w_1 = (1/\mu_j)(1 + 1/\mathfrak{C}_j)\log(1 + \mathfrak{C}_j)$ so that the error is bounded by $\int_{w_1}^\infty (w+1)^{-\theta} dw = (\theta - 1)^{-1}(w_1 + 1)^{-(\theta-1)}$. In view of this correction term, we take our inner integral to be of the form

$$\int_0^\infty \frac{[1 + \mathfrak{C}_j \exp(-\mu_j w)]^\rho}{(w+1)^\theta} dw \approx \frac{(1 + \mathfrak{C}_j)^{\rho+1}}{(\theta - 1) + \mathfrak{C}_j((\theta - 1) + \rho\mu_j)}, \tag{154}$$

which, in addition to being an improvement of the approximation (as determined numerically), is exact when $\mathfrak{C}_j = 0$. Substituting this expression into Eq. (152) yields

$$P_j \approx \frac{1}{c_j} \int_0^{\frac{\lambda' c_j}{2\tau^{\alpha/2}}} \frac{[1 + (K_j - 1)e^{-\mu}]^{(\rho+1)\beta}}{1 + (K_j - 1)e^{-\mu}(1 + \frac{\rho\mu\alpha}{2})} d\mu \tag{155}$$

in terms of the original variables. This formula is very accurate when ρ is large ($\geq$ 15 say) and θ is moderate ($\geq$ 5 say), i.e., α is not large ($\leq$ 0.5 say). Although the above analysis was done for the case $\alpha > 0$, Eq. (155) is well defined even if $\alpha = 0$. Indeed, for $\alpha = 0$ it collapses to the integral in Eq. (151). Furthermore, when $\lambda' \geq \lambda$ we can approximate Eq. (155) in a manner similar to the approach used to evaluate the inner integral above to obtain

$$P_j \approx \frac{1}{c_j} \frac{K_j^{\rho\beta+1}}{(K_j - 1)} \chi \tag{156}$$

where

$$\chi = \frac{1}{\beta(\rho + 1)} \left[1 + \frac{1 + \rho\alpha/2}{\rho + 1}\right]. \tag{157}$$

The error involved in the approximation of the outer integral is larger than that for the inner integral since the rate of decay $(\rho + 1)\beta$ of the dominant term, $[1 + (K_j - 1)e^{-\mu}]^{(\rho+1)\beta}$ is typically much smaller than ρ, which was the decay rate in the inner integral. This leaves asymptotic approximations such as the ones above focusing near the origin somewhat less accurate (Copson (1965)). Therefore, in our numerical calculations we numerically integrate Eq. (154) instead of using Eq. (156). Nonetheless Eq. (156) is valuable since it captures in closed form the cumulative hazard ahead of a cluster of j breaks, except perhaps for a scale constant, and can be used in a closed form evaluation of $W_k(\tau)$ in Section 7.

In simplified form we finally have the key approximation

$$\begin{aligned} W_k(\tau) &\approx 2^{k-1}\Gamma(1 + \beta)^k \Gamma(1 + k\beta)^{-1} \pi_\infty^{k\rho\beta} \tau^{k(\beta+\alpha/2)} \prod_{j=0}^{k-1} N_j P_j \\ &\approx (2\chi)^{k-1}\Gamma(1 + \beta)^k \Gamma(1 + k\beta)^{-1} \pi_\infty^{k\rho\beta} \tau^{k(\beta+\alpha/2)} \frac{\lambda}{\tau^{\alpha/2}} \prod_{j=1}^{k-1} \frac{N_j}{c_j} \frac{K_j^{\rho\beta+1}}{K_j - 1} \end{aligned} \tag{158}$$

where in the second step, we have extracted the anomalous $j = 0$ factor $\lambda/\tau^{\alpha/2}$ from the product series. Unlike the other factors, this

factor corresponds to the initial break or the *seed* of the k-cluster, the probability of its inception, given by Eq. (47) is therefore independent of α since matrix creep has no time to occur.

C. Closed form Approximation for $W(\tau)$ in 2D

We now determine a closed form approximation for the weak-linked lifetime distribution function $W(\tau)$. We begin with Eq. (64) with $N_j = 2$, $j = 1, 2, \ldots, k-1$.

$$W_k(\tau) = \tau^{k(\beta+\alpha/2)} \frac{\Gamma^k(\beta+1)}{\Gamma(k\beta+1)} (4\chi)^{k-1} \pi_\infty^{k\rho\beta} \frac{\lambda}{\tau^{\alpha/2}} \prod_{j=1}^{k-1} \left[\frac{1}{1+\frac{1}{\sqrt{j}}} \frac{K_j^{\rho\beta+1}}{K_j - 1} \right] \tag{159}$$

We let $a = \pi\psi/8$ so that $K_j = \sqrt{1+aj}$. In terms of a we have excellent approximations for the various factors in Eq. (159) as

$$\prod_{j=1}^{k-1} \frac{1}{1+\frac{1}{\sqrt{j}}} \approx \frac{k^{k/2}}{(\sqrt{k}+1)^{k-1}} e^{-(\sqrt{k}-1)}, \tag{160}$$

$$\prod_{j=1}^{k-1} K_j \approx \left[\frac{(ak+1)^{k+\frac{1}{a}-\frac{1}{2}}}{(a+1)^{\frac{1}{a}+\frac{1}{2}}} e^{-(k-1)} \right]^{\frac{1}{2}}, \tag{161}$$

and,

$$\prod_{j=1}^{k-1} (K_j - 1) \approx a^{\frac{k-1}{2}} \frac{\left(\sqrt{k+\frac{1}{a}} - \sqrt{1+\frac{1}{a}}\right)^{k-\frac{1}{2}}}{\sqrt{1+\frac{1}{a}} - \sqrt{1+\frac{1}{a}}} e^{-\frac{1}{2}(k-1)} \times e^{-\sqrt{\frac{1}{a}}\left\{\sqrt{k+\frac{1}{a}} - \sqrt{1+\frac{1}{a}}\right\}}. \tag{162}$$

Setting

$$W_k(\tau) = W_{k+1}(\tau) \tag{163}$$

yields the intersection time of the W_k and W_{k+1} lines as

$$\tau^{\beta+\alpha/2} = \left(1 + \frac{1}{\sqrt{k}}\right) \frac{1}{4\chi} \frac{K_k - 1}{K_k^{\rho\beta+1}} \frac{\Gamma((k+1)\beta+1)}{\Gamma(\beta+1)\Gamma(k\beta+1)} \frac{1}{\pi_\infty^{\rho\beta}} \tag{164}$$

Algebraic manipulations following the substitution of Eq. (160), Eq. (161), Eq. (162), and Eq. (164) in Eq. (159) result in

$$W_k = \frac{\theta_1}{\tau^{\alpha/2}} \left(k + \frac{1}{a}\right)^{\theta_2} \exp\left\{ -\left(\frac{\rho}{2} - 1\right) \beta \left(k + \frac{1}{a}\right) (1 - \Theta_k) \right\} \tag{165}$$

where

$$\theta_1 = \frac{\lambda}{4\chi}\frac{\sqrt[4]{a}\left[\sqrt{1+a}-1\right]^{1/2}}{(1+a)^{\frac{\rho\beta+1}{2}}}\left(\frac{a}{1+a}\right)^{\theta_2} \times \exp\left\{\left(\frac{\rho}{2}-1\right)\beta(1+\frac{1}{a})+\sqrt{\frac{1}{a}}\sqrt{1+\frac{1}{a}}+2\right\}, \tag{166}$$

$$\theta_2 = \left(\frac{1}{a}-\frac{1}{2}\right)\frac{\rho\beta+1}{2}, \tag{167}$$

and

$$\Theta_k = \frac{\sqrt{1/a}-1}{\beta(\rho/2-1)}\left(k+\frac{1}{a}\right)^{-\frac{1}{2}}. \tag{168}$$

Inverting Eq. (164), we get an expression for k in terms of τ as

$$k+\frac{1}{a} \approx \frac{\theta_3}{\tau^{\theta_4}} \tag{169}$$

where

$$\theta_3 = \left(\frac{3\beta^{\beta}\pi_{\infty}^{-\rho\beta}}{16\chi a^{\rho\beta/2}\Gamma(1+\beta)}\right)^{\frac{2}{(\rho-2)\beta}},$$

and

$$\theta_4 = \frac{2}{(\rho-2)\beta}(\beta+\alpha/2)$$

Substituting Eq. (169) into Eq. (165) we finally have the key result

$$W(\tau) = \frac{\theta_1\theta_3^{\theta_2}}{\tau^{\theta_5}}\exp\left\{-\left(\frac{\rho}{2}-1\right)\beta\frac{\theta_3}{\tau^{\theta_4}}(1-\Theta(\tau))\right\} \tag{170}$$

where

$$\theta_5 = \theta_2\theta_4 - \alpha/2,$$

and

$$\Theta(\tau) = \frac{\sqrt{1/a}-1}{(\rho/2-1)\beta}\frac{\tau^{\theta_4/2}}{\sqrt{\theta_3}}.$$

D. Closed form Approximation for $W(\tau)$ in 3D

Proceeding as in 2D we start by specializing Eq. (64) for 3D to

$$W_k(\tau) = \tau^{k(\beta+\alpha/2)}\frac{\Gamma^k(\beta+1)}{\Gamma(k\beta+1)}\chi^{k-1}\pi_{\infty}^{k\rho\beta}\frac{\lambda}{\tau^{\alpha/2}} \prod_{j=1}^{k-1}\left[\frac{\eta j^{\nu}}{1+\frac{1}{\sqrt[4]{j}}}\frac{K_j^{\rho\beta+1}}{K_j-1}\right]. \tag{171}$$

We let $a = 2\psi/\pi^{3/2}$ so that $K_j = \sqrt{a\sqrt{j}+1}$, and as in 2D, we first approximate the different products in Eq. (171) to yield

$$\prod_{j=1}^{k-1} \eta j^{\nu} \approx (2\pi)^{\frac{\nu}{2}} \eta^{k-1} e^{-\nu k} k^{\nu(k-\frac{1}{2})}, \tag{172}$$

$$\prod_{j=1}^{k-1} \frac{1}{1+\frac{1}{\sqrt[4]{j}}} \approx \frac{k^{k/4}}{(\sqrt[4]{k}+1)^{k-1}} \exp\left\{-\frac{k^{3/4}}{3} + \frac{k^{1/2}}{2} - k^{1/4} + \frac{2}{3}\right\}, \tag{173}$$

$$\prod_{j=1}^{k-1} K_j \approx \left[\frac{(a\sqrt{k}+1)^{k-\frac{1}{a^2}-\frac{1}{2}}}{(a+1)^{\frac{1}{2}-\frac{1}{a^2}}} \exp\left\{-\frac{k}{4} + \frac{\sqrt{k}}{2a} + \frac{1}{2}\left[\frac{1}{2} - \frac{1}{a}\right]\right\}\right]^{\frac{1}{2}}, \tag{174}$$

and

$$\prod_{j=1}^{k-1} K_j - 1 \approx \frac{(\sqrt{a\sqrt{k}+1}-1)^{k-\frac{1}{2}}}{(\sqrt{a+1}-1)^{\frac{1}{2}}} \exp\left\{-\frac{k-1}{4} + \right.$$
$$\left. \times \frac{2}{3a^2}\left[\sqrt{a\sqrt{k}+1} - \sqrt{a+1}\right] - \frac{1}{3a}\left[\sqrt{k}\sqrt{a\sqrt{k}+1} - \sqrt{a+1}\right]\right\}. \tag{175}$$

As in 2D, setting

$$W_k(\tau) = W_{k+1}(\tau) \tag{176}$$

gives τ in terms of k as

$$\tau^{\beta+\alpha/2} = \left(1 + \frac{1}{\sqrt[4]{k}}\right) \frac{1}{\eta\chi k^{\nu}} \frac{K_k - 1}{K_k^{\rho\beta+1}} \frac{\Gamma((k+1)\beta+1)}{\Gamma(\beta+1)\Gamma(k\beta+1)} \frac{1}{\pi_{\infty}^{\rho\beta}}. \tag{177}$$

Substituting Eq. (172 – 177) into Eq. (171) and simplifying yields

$$W_k \approx \frac{\theta_1}{\tau^{\alpha/2}} \left[\sqrt{k} + \frac{1}{a}\right]^{-\theta_2} \exp\left\{-\left(\frac{\rho\beta}{4} - \beta + \nu\right)\left[\sqrt{k} + \frac{1}{a}\right]^2 (1 - \Theta_k)\right\} \tag{178}$$

where

$$\theta_1 = \frac{\lambda(2\pi)^{\frac{\nu-1}{2}}}{\eta\chi} \frac{e^{\beta+\frac{1}{2}}}{\sqrt{\beta}} (\sqrt{a+1}-1)^{\frac{1}{2}} \frac{a^{-\frac{\rho\beta+1}{2}\left(\frac{1}{a^2}+\frac{1}{2}\right)+\frac{1}{4}}}{(a+1)^{\frac{\rho\beta+1}{2}\left(\frac{1}{2}-\frac{1}{a^2}\right)}}$$
$$\times \exp\left[\frac{\sqrt{a+1}}{3a^2}(2-a) + \frac{\rho\beta}{4a^2}(a-1)^2 + \frac{\beta-\nu+\frac{1}{2}}{a^2} + \frac{2}{3}\right], \tag{179}$$

$$\theta_2 = \frac{\rho\beta+1}{2}\left(\frac{1}{a^2} - \frac{1}{2}\right) + \nu + \frac{1}{4}, \tag{180}$$

and

$$\Theta_k \approx \frac{4a}{\rho\beta - 4(\beta-\nu)}\left(\sqrt{k}+\frac{1}{a}\right)^{-\frac{1}{2}} - \frac{4(\rho\beta - 2(\beta-\gamma)-\frac{5}{6})}{a(\rho\beta-4(\beta-\nu))}\left(\sqrt{k}+\frac{1}{a}\right)^{-1} \times \frac{2(1-4/(3a^{3/2}))}{\rho\beta-4(\beta-\nu)}\left(\sqrt{k}+\frac{1}{a}\right)^{-\frac{3}{2}}. \tag{181}$$

Inverting Eq. (177) we get

$$\sqrt{k}+\frac{1}{a} \approx \frac{\theta_3}{\tau^{\theta_4}} \tag{182}$$

where

$$\theta_3 = \left(\frac{3\beta^\beta \pi_\infty^{-\rho\beta}}{4\eta\chi a^{\rho\beta/2}\Gamma(\beta+1)}\right)^{\frac{2}{\rho\beta-4(\beta-\nu)}}, \tag{183}$$

and

$$\theta_4 = \frac{2\beta+\alpha}{\rho\beta-4(\beta-\nu)}. \tag{184}$$

Upon substituting Eq. (182) into Eq. (178) we finally get

$$W(\tau) \approx \frac{\theta_1 \tau^{\theta_5}}{\theta_3^{\theta_2}} \exp\left\{-\left(\frac{\rho\beta}{4}-\beta+\nu\right)\frac{\theta_3^2}{\tau^{2\theta_4}}(1-\Theta(\tau))\right\} \tag{185}$$

where

$$\theta_5 = \theta_2\theta_4 + \alpha/2, \tag{186}$$

and

$$\Theta(\tau) \approx \frac{4a\theta_3^{-1/2}}{\rho\beta-\beta+\nu}\tau^{\theta_4/2} - \frac{4(\rho\beta-2(\beta-\gamma)-\frac{5}{6})}{a\theta_3(\rho\beta-4(\beta-\nu))}\tau^{\theta_4} + \frac{2(1-4/(3a^{3/2}))}{\theta_3^{3/2}(\rho\beta-4(\beta-\nu))}\tau^{3\theta_4/2}. \tag{187}$$